Journal of CO2 Utilization 103 (2026) 103302

Contents lists available at ScienceDirect

Journal of CO2 Utilization

journal homepage: www.elsevier.com/locate/jcou

Solar photothermo-catalytic CO_2 conversion into methane: Effect of phyllosilicates on the performance of Ni-Zn-Al layered double hydroxide-derived catalysts

Luca Calantropo [a], Eleonora La Greca [a,b], Leonarda Francesca Liotta [b], Giuliana Impellizzeri [c], Antonino Gulino [a,d], Angelo Ferlazzo [a,d], Libera Vitiello [e], Sabrina Carola Carroccio [e], Salvatore Scirè [a], Roberto Fiorenza [a,c,*]

[a] Department of Chemical Sciences, University of Catania, V.le A. Doria 6, Catania 95125, Italy
[b] Institute for the Study of Nanostructured Materials (ISMN), National Research Council (CNR), Via Ugo La Malfa 153, Palermo 90146, Italy
[c] Institute for Microelectronics and Microsystems (IMM), National Research Council (CNR), Via S. Sofia 64, Catania 95123, Italy
[d] INSTM UdR of Catania, V.le A. Doria 6, Catania 95125, Italy
[e] Institute for Polymers, Composites and Biomaterials (IPCB), National Research Council (CNR), Via Paolo Gaifami 18, Catania 95126, Italy

ARTICLE INFO

Keywords:
Photothermo-catalysis
Layered double hydroxide-derived catalyst
CO_2 methanation
Phyllosilicates

ABSTRACT

The development of efficient catalysts for CO_2 utilization is a key challenge for industrial sustainability. This study explores the photothermo-catalytic methanation of CO_2 using Ni-Zn-Al Layered Double Hydroxide-derived (LDHd) catalysts modified with phyllosilicates (Montmorillonite K30 and Halloysite). LDH precursors were synthesized by co-precipitation and hydrothermal treatment, then calcined and reduced leading to the formation of mixed oxides and metallic Ni and Zn nanoparticles. Catalytic performances were evaluated at 1 atm and 350 °C. The Ni-Zn-Al LDHd catalyst achieved high CO_2 conversion (86 %) and CH_4 selectivity (>99 %) under photothermo-catalytic conditions, outperforming commercial Ni systems. Incorporation of halloysite, thermally treated at 200 °C, further increased CO_2 conversion to 92 % with the same high CH_4 selectivity. This improved performance is attributed to enhanced surface area, optical absorption and moderate–strong basic sites from LDHd–Halloysite interaction. In contrast, Montmorillonite modification, despite cetyltrimethylammonium bromide (CTAB) intercalation, resulted in lower activity and selectivity, due to weaker basicity and ineffective LDHd interaction. The Ni-Zn-Al LDHd/halloysite catalyst exhibited excellent stability during 20 h of continuous photothermo-catalytic test at 350 °C. These results demonstrate the potential of phyllosilicate-modified LDH-derived catalysts, with low metals content, for efficient CO_2 methanation under solar irradiation.

1. Introduction

The development of sustainable processes and materials for the environmental protection is an important target in the field of catalysis and industrial chemistry. Among the recent technologies, the capture and the utilization of CO_2 (CCU) for the production of fuels and chemicals are fascinating processes [1–3]. The constant emission of carbon dioxide indeed, strongly contributes to the increase of the greenhouse effect and it is related to the global warming and climate change phenomena. In 2022 the global emissions of CO_2 from the use of fossil fuels and industrial production have reached 36.1 ± 0.3 Gt CO_2. In order to reduce the emissions, it is necessary to investigate new technologies and materials that allow the re-use and the exploitation of CO_2 [4,5].

Among the various CO_2 conversion technologies, the thermocatalytic hydrogenation reaction is one of the most promising, leading to the production of light alkanes, olefins, alcohols and other hydrocarbons [6,7]. Carbon dioxide is a thermodynamically stable molecule with two double linear bonds. Therefore, the catalytic hydrogenation reaction, which involves the breaking of such double bonds, requires a rather high activation energy (about 239 kJ/mol) with operating temperature between 250 °C and 550 °C and pressure between 1 and 100 bar, depending on the used catalyst. For these reasons the hydrogenation is considered a highly energy-intensive process [4,8]. The CO_2 methanation, or Sabatier reaction (reaction 1), on the contrary requires less hard

* Corresponding author at: Department of Chemical Sciences, University of Catania, V.le A. Doria 6, Catania 95125, Italy.
E-mail address: rfiorenza@unict.it (R. Fiorenza).

https://doi.org/10.1016/j.jcou.2025.103302
Received 24 September 2025; Received in revised form 21 November 2025; Accepted 11 December 2025
Available online 16 December 2025

conditions then other hydrogenation pathways [8]. In fact, different studies demonstrate that the methanation reaction is favoured by a decrease in pressure as it leads to a decrease in the number of gaseous molecules, so it can also occurs at ambient pressure [9]. In addition, the exothermic nature of the reaction makes it thermodynamically favoured at low temperatures. However, the activation of stable molecules such as CO_2 and H_2 requires temperatures higher than 250 °C [8].

The typical reactions involved in the CO_2 methanation process are:

1) Methanation: $CO_2 + 4\,H_2 \leftrightarrow CH_4 + 2\,H_2O (\Delta H_R^\circ = -165 kJmol^{-1})$

2) Reverse water gas shift (RWGS): $CO_2 + H_2 \leftrightarrow CO + H_2O (\Delta H_R^\circ = 41 kJmol^{-1})$

3) CO methanation: $CO + 3\,H_2 \leftrightarrow CH_4 + H_2O (\Delta H_R^\circ = -206 kJmol^{-1})$

A significant disadvantage of the Sabatier reaction is represented by the low selectivity, which is a function of various parameters such as temperature, employed catalyst, CO_2/H_2 ratio, quantity of water in the reaction environment, etc. This can result in a major production of carbon monoxide (CO), obtained by reverse water gas shift (reaction 2), which is favoured at high temperature, instead of methane [9]. Another important drawback is represented by the water production, that can lead to the deactivation of the catalyst due to its adsorption that can cause the blockage of the catalyst pores [10]. The presence of water can also modify the selectivity favouring the reverse water gas shift reaction (reaction 2) or other hydrogenation pathways leading to different by-products [11].

These drawbacks can be overcome with a photo(solar)-thermocatalytic approach. This involves the synergistic use of thermal energy and solar radiation in order to activate the photothermal-catalyst enabling milder conditions with an energy saving process [12,13].

In addition, the photothermo-catalysis can be an efficient solution for the excessive water production. Indeed, towards the photocatalytic mechanism, the water molecules, adsorbed on the surface of the catalyst, can interact with the holes of the photothermo-catalyst (generally a semiconductor), generated by the absorption of the solar irradiation, favouring the formation of protons. These protons can interact directly with adsorbed CO_2 or they can be reduced by the photoelectrons, promoted in the conduction band of the photothermo-catalyst, allowing the formation of H_2 which can further favour the CO_2 methanation reaction [14–16].

In our previous study, we have investigated the performance in the photothermo-catalytic CO_2 Sabatier reaction of Co-Zn-Al and Co-Mg-Al Layered Double Hydroxides (LDHs)-derived catalysts and their interaction with a semiconductor photocatalyst as the silicon carbide (SiC). The SiC/Co-Zn-Al catalyst demonstrated enhanced photothermo-catalytic activity, achieving a good CH_4 selectivity (70 %) and CO_2 conversion (65–70 %) at lower temperatures (350 °C) than the bare thermocatalytic process [13]. In order to improve the performance of this type of photothermo-catalysts we investigate in this work, new LDH-derived catalyst compositions. In addition, we have studied their interactions with sustainable materials as the phyllosilicates, rather than critical or expensive semiconductors. The advantage of using catalysts derived from LDH precursors consists in obtaining a highly homogeneous mixed oxide that gives better catalytic performance than those obtained by a physical mixture of the commercial oxides [13,17]. The high dispersion of the metal species promotes cooperation between the different active sites thus avoiding the aggregation and sintering phenomena which lead to the deactivation of the catalyst. In addition, the LDH-derived catalysts can partially maintain the layered structure, this favours the adsorption of CO_2 and affects the optical and textural properties of the material. Finally, the possibility of carrying out the synthesis of LDH in the presence of other catalytic supports, as the phyllosilicates, makes the production of the composite materials simple and effective. In this way the interaction between the two materials is promoted within the formation of hybrid structures with peculiar morphologies, obtained modifying simple reaction parameters such as temperature, oversaturation conditions, etc. [18]. The use of natural phyllosilicates offers notable advantages over conventional supports such as SiO_2, Al_2O_3 and SiC in CO_2 methanation. The high surface area, layered or fibrous morphology and elevated cation-exchange capacity of the phyllosilicates enable superior metal dispersion and stronger metal–support interactions, significantly reducing sintering respect to the most used supports [19]. Studies on Ni/phyllosilicates catalysts report improved CO_2 activation, enhanced reducibility control and superior stability compared to Ni/SiO_2 or Ni/Al_2O_3 systems. Moreover, the tuneable acidic and basic sites and abundant surface silanol groups in phyllosilicates help to stabilize reaction intermediates, maintaining simultaneously a high CH_4 selectivity. Furthermore, their low cost and natural availability make them attractive and scalable alternatives [20,21].

Recent studies have highlighted the potential of photo-thermal catalysis for the Sabatier reaction. *Steeves and Esser-Kahn* [22] demonstrated that Ni nanoparticles can drive the Sabatier reaction under solar irradiation, using local photo-induced heating to achieve high CO_2 conversion at lower temperatures than conventional thermocatalytic route. *Xiao et al.* [23] reported a Ni/TiO_2 Mott–Schottky heterojunction catalyst, where synergistic photo-generated charge carriers and local heating enhance the CH_4 selectivity and the reaction rates. However, these studies rely on semiconducting materials or catalysts with high metal loadings, which are often costly, synthesis-intensive and environmentally challenging. In contrast, our work shows that naturally occurring phyllosilicates can act as low-cost and eco-friendly supports, effectively tuning the photothermal and surface properties of LDH-derived catalysts, even with a reduced amount of metals, therefore enhancing both light-driven and thermally driven contributions in CO_2 methanation reaction.

Based on the above consideration, in this work we tested different composition of LDH-derived catalysts (Ni-Zn-Al). In particular, Aluminium is one of the most typical M^{3+} cations in the structure of LDH and favour the CO_2 adsorption [24,25]. The presence of Ni was fundamental to promote the catalytic activity at low temperatures, and it is more selective towards methane and less expensive than other transition metals as Co [26]. Whereas the presence of Zn is essential to activate the photocatalytic contribution during the photothermal tests with the formation of ZnO/Zn-based spinel structures [13].

Moreover, the influence of the addition of phyllosilicates employed as support of the Ni-Zn-Al LDH-derived catalyst was investigated. Specifically, the Halloysite and the Montmorillonite were used after different activation processes. These low-cost and environmentally friendly natural clays can improve the surface area of the catalyst and the dispersion of metallic species promoting both the activity and the stability of the catalyst, avoiding sintering and aggregation phenomena [20].

It is important to underline that all the tested composite materials (Ni-Zn-Al LDH/phyllosilicates-derived catalysts) present a lower amount of active metal species compared to the bare Ni-Zn-Al LDH-derived catalyst. A limited use of metals is a fundamental strategy in the design of new catalysts with high performance and low environmental and economic impact [11,20].

2. Material and methods

2.1. Samples preparation

The $Ni(NO_3)_2{\cdot}6H_2O \geq 98$ % was furnished by Fluka; $Al(NO_3)_3{\cdot}9H_2O \geq 99$ % by Carlo Erba; $Zn(NO_3)_2{\cdot}6H_2O \geq 98$ % by Sigma Aldrich; anhydrous Na_2CO_3, ≥ 99.9 % by Sigma Aldrich; NaOH ≥ 99 % pellets by Panreac; $HNO_3 \geq 65$ % by Honeywell/Fluka; Montmorillonite K30 by Sigma-Aldrich; Halloysite nanoclay by Aldrich Chemistry; Cetyltrimethylammonium bromide (CTAB) by Sigma Aldrich. All the reagents were used as purchased without further steps of purification.

2.1.1. Synthesis of Ni-Zn-Al layered double hydroxide-derived catalyst

The synthesis of the Ni-Zn-Al LDH precursor was carried out by coprecipitation method and subsequent hydrothermal treatment. The precursors used were the corresponding metal nitrates, i.e., 2.52 g of Ni $(NO_3)_2{\cdot}6H_2O$, 0.75 g of $Zn(NO_3)_2{\cdot}6H_2O$ and 1.5 g of $Al(NO_3)_3{\cdot}9H_2O$. They were mixed and solubilised in 10 mL of deionized water. The amount of each metal was chosen in order to have a nominal atomic concentration ratio of $\frac{Ni+Zn}{Al} = 3$.

Additionally, at this solution containing the metal cations it was slowly added 15 mL of an aqueous solution in which 1.2 g of sodium hydroxide NaOH and 0.6 g of anhydrous sodium carbonate Na_2CO_3 were previously mixed and solubilized. The pH of the resultant solution was maintained between 8 and 9 by the addition of HNO_3 (1 M). Afterwards, the resultant solution was transferred in a Teflon lined-autoclave and heated at 120 °C for 20 h. The obtained slurry was separated by centrifugation (8000 rpm, 10 min) and washed with deionized water. Finally, the precipitate was dried at 80 °C overnight and then calcined at 600 °C for 6 h in order to obtain a highly homogeneous mixed oxides catalyst derived from the LDH precursor. This sample was coded as Ni-Zn-Al LDHd (Ni-Zn-Al Layered double hydroxide-derived catalyst).

2.1.2. Ni-Zn-Al LDHd + montmorillonite composites synthesis

The synthesis of the Ni-Zn-Al LDH modified with Montmorillonite K30 (MMT) was carried out with the same coprecipitation method described before but in presence of montmorillonite K30 in different quantities, in order to obtain weight ratios LDH:MMT of 1:1 and 2:1. The samples were coded as Ni-Zn-Al LDHd + MMT (1:1) and Ni-Zn-Al LDHd + MMT (2:1). Two other samples were prepared using montmorillonite K30 activated by intercalation of CTAB [27]. Specifically, 5 g of montmorillonite and 5 g of CTAB were suspended in 200 mL of deionized water. This solution was stirred, refluxed and heated at 80 °C for 24 h. It was then filtered and thoroughly washed with deionised water. The obtained powders were dried at 80 °C for 12 h. Afterwards, on the activated K30 with CTAB were added by coprecipitation the Ni-Zn-Al LDH precursors following the same procedures reported above. These samples were coded as Ni-Zn-Al LDHd + MMT-CTAB (1:1) and Ni-Zn-Al LDHd + MMT-CTAB (2:1).

2.1.3. Ni-Zn-Al LDHd + halloysite composites synthesis

The synthesis of the Ni-Zn-Al LDH modified with Halloysite (HAL) was carried out by coprecipitation method in presence of Halloysite nanoclay to obtain a weight ratios LDH:HAL of 2:1. Four composite catalysts were synthesized using halloysite as purchased, and HAL thermically treated at 200 °C, 400 °C and 600 °C in order to modify the interaction between the halloysite and the LDH, and the dispersion of LDH on HAL, as well as the morphology of the final composites [28].

For the HAL thermal treatments, 1.5 g of bare halloysite was placed in a quartz tubular reactor and introduced in tubular oven under Ar flow for 4 h. Successively, on the obtained HAL powders were added the Ni-Zn-Al LDH precursors by co-precipitation following the same procedures reported above.

The obtained samples were coded as Ni-Zn-Al LDHd + HAL (2:1), Ni-Zn-Al LDHd + HAL200 (2:1), Ni-Zn-Al LDHd + HAL400 (2:1), Ni-Zn-Al LDHd + HAL600 (2:1).

Please note that in all the hybrid composites (Ni-Zn-Al LDHd + MMT and Ni-Zn-Al LDHd + HAL) the nominal atomic concentration ratio of Ni+Zn/Al was 2/3 (i.e. = 2) compared to the bare Ni-Zn-Al LDHd sample.

2.2. Samples characterization

X-ray diffraction (XRD) patterns were obtained using a Bruker D5005 diffractometer equipped with Cu Kα radiation (λ = 1.5418 Å) and a graphite monochromator positioned on the diffracted beam. Data were collected over the 2θ range of 10° to 90°, with a scanning step size of 0.02° and a counting time of 0.5 s per step. Crystalline phase identification was carried out by comparison with standard patterns from the Inorganic Crystal Structure Database (ICSD).

The morphology and chemical composition of the catalysts were analysed by Scanning Electron Microscopy (SEM) using a Zeiss Supra 25 field-emission microscope equipped with an Energy-Dispersive X-ray Spectroscopy (EDX) detector. Prior to analysis, the catalyst powders were mounted onto SEM stubs and sputter-coated with a thin gold layer (<10 nm) to enhance conductivity. EDX spectra were acquired and processed using Phenom Element Identification software (version 3.8.4.0; Phenom-World BV, Eindhoven, The Netherlands). The analyses were carried out at randomly selected regions, including three points analyses and three elemental mapping for each sample.

The N_2 physisorption measurements were performed at −196 °C using a Micromeritics Tristar II Plus 3020 analysers. Before the analysis, the samples were treated at 100 °C overnight. The specific surface area was determined using the Brunauer–Emmett–Teller (BET) method, while the pore size distribution and pore volume were evaluated using the Barrett–Joyner–Halenda (BJH) method.

Diffuse reflectance UV–Vis spectra (UV–Vis DRS) were acquired using a JASCO V-670 spectrophotometer. The optical band-gap energy (Eg) of the catalysts was estimated by plotting the modified Kubelka–Munk function against photon energy (hν) [29].

X-ray photoelectron spectra (XPS) were measured at a 45° take-off angle relative to the surface sample holder, with a PHI 5000 Versa Probe II system (ULVAC-PHI, INC., base pressure of the main chamber 1 × 10^{-8} Pa) [30,31]. Samples were excited with the monochromatized Al Kα X-ray radiation using a pass energy of 5.85 eV. The instrumental energy resolution was ≤ 0.5 eV. The XPS peak intensities were obtained after Shirley's background removal [30,31]. Spectra calibration was achieved by fixing the Ag $3d_{5/2}$ peak of a clean sample at 368.3 eV [32]. The atomic concentration analysis was performed by considering the relevant atomic sensitivity factors. The fitting of some XP spectra was carried out, using the XPSPEAK4.1 software, by fitting the spectral profiles with symmetrical Gaussian envelopes, after subtraction of the background. This process involves data refinement, based on the method of the least squares fitting, carried out until there is the highest possible correlation between the experimental spectrum and the theoretical profile. The residual or agreement factor R, defined by $R = [\Sigma (F_{obs} - F_{calc})^2 / \Sigma (F_{obs})^2]^{1/2}$, after minimization of the function $\Sigma (F_{obs} - F_{calc})^2$, converged to the value of 0.03.

CO_2 temperature-programmed desorption (CO_2-TPD) measurements were carried out in a fixed-bed quartz reactor loaded with 0.15 g of catalyst. Prior to the analysis, the samples were pretreated under helium flow (30 cc/min) at 100 °C for 1 h to remove physisorbed species. Subsequently, pure CO_2 (30 cc/min) was introduced for 60 min at 25 °C to allow adsorption and surface saturation. After saturation, the CO_2 flow was stopped and the TPD was performed under pure He (30 cc/min) by heating the sample from 30 °C to 600 °C at a ramp rate of 10 °C/min.

The desorbed CO_2 was monitored using a quadrupole mass spectrometer (Sensorlab VG Quadrupoles).

2.3. Photothermo-catalytic CO_2 methanation tests

The photothermo-catalytic CO_2 methanation tests were carried out at atmospheric pressure in a U-shaped fixed bed quartz reactor, filled with 0.2 g of catalyst, heated by an oven at 350 °C and externally irradiated with a solar lamp (Osram Ultra Vitalux 300 W, irradiance of 10.7 mW/cm^2) (Figure S1). The flows of the reactant gas mixture (CO_2 99.999 % and H_2 gas produced by a HK Hydrogen generator, purity 99.9996 %) were regulated with mass flow controllers in order to favour the formation of methane (H_2:CO_2 molar ratio 4:1) and before to start with the contextual heating and irradiation, the gases were flowed in the reactor in the dark for 1 h to reach the adsorption-desorption

equilibrium. Before the tests, the sample surface was pre-cleaned from possible carbonaceous contaminants following the procedures reported in the ref. [33] and each sample was reduced in H_2 flow (50 cc/min) at 600 °C for 4 h in order to obtain the formation of supported Ni nanoparticles able to promote the CO_2 methanation reaction [34,35]. For each reactions test CO_2, CH_4, CO and the eventual other products were examined with the GC Agilent 8860 equipped with a TCD detector and a Carboxen 1000 column, and with the Trace GC instrument with FID detector (Porapak Q column) both opportunely calibrated.

The CO_2 conversion was calculated with the following formula:

$$CO_2 conversion\% : \left(\frac{Area_{peak\ CO2in} - Area_{peak\ CO2out} \times \left(\frac{Area_{peak\ standard\ in}}{Area_{peak\ standard\ out}}\right)}{Area_{peak\ CO2in}}\right) \times 100$$

To verify the obtained values, also the mass balance method was applied, considering the following equation:

$$CO_2 conversion\% : \left(\frac{Area_{peak\ CO2out}}{Area_{peak\ products\ out} + Area_{peak\ CO2out}}\right) \times 100$$

The two calculations were in accordance with each other (± 5 %, reproducibility 95 %).

The CH_4 selectivity was estimated as follows:

$$CH_4 selectivity\% : \left(\frac{[CH_4]_p}{CO_2 conversion}\right) \times 100$$

where $[CH_4]_p$ is the molar concentration of produced CH_4 determined by TCD after standard calibration [36].

The temperature was monitored with an infrared thermal camera and a thermocouple. The thermocatalytic tests were carried out with the same set-up without using the solar lamp, while the photocatalytic tests were carried out without using the oven for heating. In both photocatalytic and photothermo-catalytic tests, the reactor was surrounded with aluminium foils in order to reflect the radiation coming from the lamp to promote a better light absorption on the catalyst bed as well as to favour a constant temperature in all the reactor profile. With this set-up, in the bare photocatalytic tests the reactor temperature was 200 °C.

3. Results and discussion

3.1. Performance of Ni-Zn-Al LDHd

The catalytic activity of the Ni-Zn-Al LDH-derived catalyst was tested in photocatalytic (P), thermocatalytic (T) and photothermo-catalytic (PT) CO_2 methanation reaction for 5 h (Fig. 1A and B) at ambient pressure and temperature of 350 °C.

Please note that in the bare solar photocatalytic test (i.e. without external heating) the reached temperature was 200 °C (experimental set-up described in the paragraph 2.3).

Under our experimental conditions CO and CH_4 were the only reaction products detected. From the Fig. 1 A it is possible to note that the CO_2 conversion in the thermocatalytic process (red line) reached a stable value of 78 % while in the photothermo-catalytic approach (green line) a higher value was achieved (around 86 %). The photocatalytic test (yellow line) gave significantly lower values, below 10 % of CO_2 conversion. This is probably due to the temperature reached during the photocatalytic test (200 °C) which did not allow an effective activation of CO_2. Regarding the selectivity trends (Fig. 1B), values above 99 % were obtained in both thermocatalytic and photothermo-catalytic approaches; on the contrary, the photocatalytic test showed a low selectivity to methane (about 5 %), favouring instead the formation of CO.

All the obtained results are in line with the thermodynamic equilibrium of the CO_2 methanation reaction which provides a maximum conversion of 93 % with 100 % of methane selectivity at 350 °C [13,37]. The photothermo-catalytic performance of the Ni-Zn-Al LDHd was

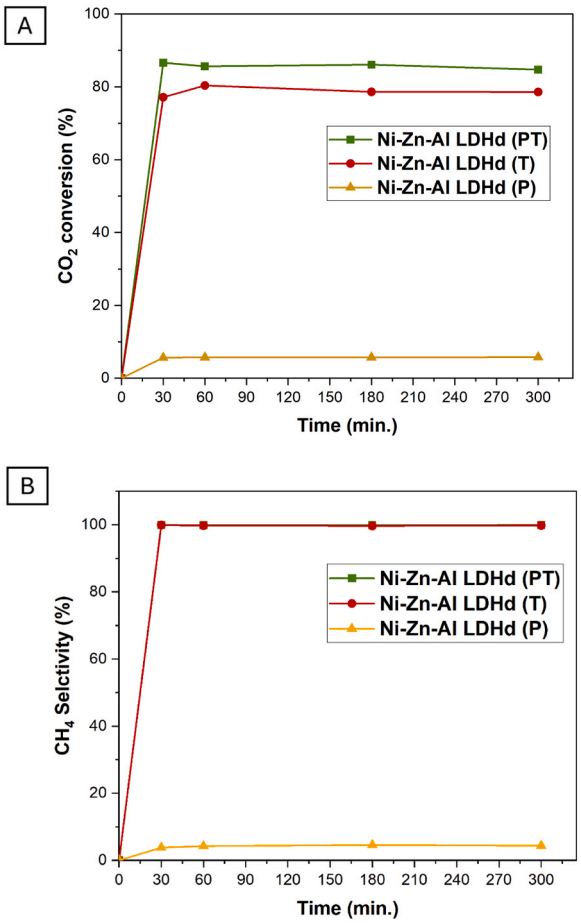

Fig. 1. CO_2 conversion (A) and CH_4 selectivity (B) for Ni-Zn-Al LDHd catalyst tested in Photothermo-catalytic (PT), Thermocatalytic (T) and Photocatalytic (P) CO_2 methanation reaction at atmospheric pressure. The reaction temperature was 350 °C for the PT and T processes, whereas for the P process the temperature was 200 °C (reached only with the use of the solar lamp).

however higher compared to the catalytic activity reported for the commercial Ni/Al_2O_3 based catalysts. Typically, with a thermocatalytic approach, using catalysts with a Ni content of about 20 wt%, under atmospheric pressure and temperature of 350 °C (conditions similar to those of this work), CO_2 conversion values between 50 % and 70 % with a CH_4 selectivity between 95 % and 100 % were measured [38–40]. In addition, the conversion values achieved with the photothermo-catalytic approach were higher than the sum of the conversion values obtained with the bare thermocatalysis and photocatalysis; therefore, it is possible to claim that the photothermo-catalytic reaction proceeds according to a synergistic photo-thermo co-catalytic mechanism [41]. This mechanism arises from the combined effect of photogenerated charge carriers and thermal energy supplied by the external heating, enhancing the reaction performance more than the bare sum of the contributions of thermocatalysis and photocatalysis. On the basis of the literature, this photo-thermo co-catalytic mechanism, is distinct from a purely photo-driven thermocatalytic mechanism, which relies primarily on thermal energy produced directly from the conversion of incident solar radiation [41,42].

To compare catalyst performance across the three processes under the same temperature, additional thermocatalytic and photothermo-catalytic tests were performed with the catalyst bed maintained at 200 °C. As shown in Figure S2, the photocatalytic and photothermo-catalytic processes exhibited similar CO_2 conversion (6 %), as expected: at a fixed reaction temperature of 200 °C, the thermal contribution is not sufficient to activate the CO_2, weakening the synergy between light-driven and

heat-driven mechanisms whereas at higher temperatures enhances the photothermo-catalytic activity. Furthermore, in the bare thermocatalytic test a slight decrease in activity (from 6 % to 5 %) was detected compared to the other approaches, consistent with the absence of any photocatalytic activation, leaving the reaction driven only by the not sufficient thermal energy. For these reasons we worked at higher temperatures (350 °C) in order to efficiently exploit the photothermo-catalytic synergistic mechanism.

3.2. Performance of Ni-Zn-Al LDHd modified with Montmorillonite K30

Considering the higher performance of Ni-Zn-Al LDHd under the photothermo-catalytic conditions, the other composites were compared only with this approach.

The catalytic results for the Ni-Zn-Al LDHd + MMT (2:1) (purple line) and Ni-Zn-Al LDHd + MMT-CTAB (2:1) (orange line) samples are shown in the Fig. 2A and B in terms of CO_2 conversion and CH_4 selectivity respectively. In the figures the results for photothermo-catalytic test of Ni-Zn-Al LDHd (green line) are also reported for a comparison with the MMT-modified catalysts.

It is possible to observe that the use of MMT K30 reduced drastically the activity of the catalyst in terms of CO_2 conversion (from 86 % of the bare Ni-Zn-Al LDHd to 25 % of the MMT-modified catalysts); this result can be due to the reduced amount of active metal species present in the Ni-Zn-Al LDHd + MMT (2:1) compared to the pure Ni-Zn-Al LDHd. However, the activity drop can be also related to the poor interaction between the LDHd and the MMT support. For this reason, an activation pretreatment of the MMT was carried out using CTAB. This led to an increase in the activity of the catalyst (from 25 % of the Ni-Zn-Al LDHd + MMT (2:1) to 45 % of Ni-Zn-Al LDHd + MMT-CTAB (2:1)) that can be associated to a double-confined effect of MMT and LDHd [27]. However, in any case, the CO_2 conversion was significantly lower compared to the bare Ni-Zn-Al LDHd catalyst and as shown in Fig. 2B, the CH_4 selectivity was lower (95 %, instead of 99 % of Ni-Zn-Al LDHd). The catalytic performance of the samples Ni-Zn-Al LDHd + MMT-CTAB (1:1) and Ni-Zn-Al LDHd + MMT (1:1) are not discussed due to their negligible activity. For this reason, the composites with the halloysite were synthesized only with a LDH:phyllosilicate weight ratio of 2:1.

3.3. Performance of Ni-Zn-Al LDHd modified with Halloysite

The results of the CO_2 photothermo-catalytic methanation for the samples Ni-Zn-Al LDHd + HAL (2:1) (yellow line), Ni-Zn-Al LDHd + HAL200 (2:1) (cyan line), Ni-Zn-Al LDHd + HAL400 (2:1) (purple line) and Ni-Zn-Al LDHd + HAL600 (2:1) (wine line) are shown in Fig. 3A and 3B, in terms of CO_2 conversion and CH_4 selectivity respectively.

The Ni-Zn-Al LDHd + HAL200 (2:1) sample, containing the halloysite pretreated at 200 °C, achieved a conversion value of 92 %, exceeding the performance of the bare Ni-Zn-Al LDHd catalyst despite the lower content of metal species. The activities of the samples containing halloysite pretreated at 400 °C and untreated HAL were initially lower (CO_2 conversion of 65–70 %) than the pure Ni-Zn-Al LDHd but after 5 h of contextual irradiation and heating they reached the same

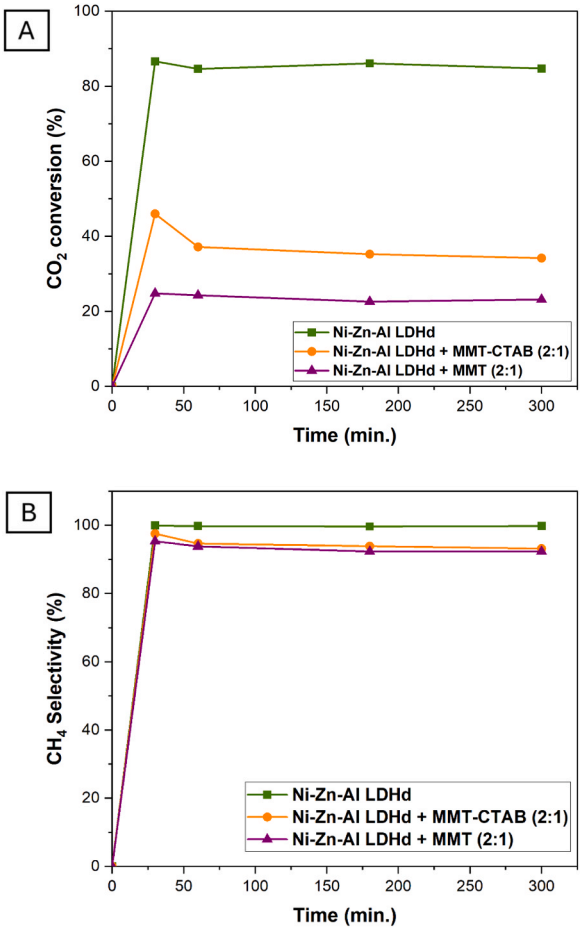

Fig. 2. CO_2 conversion (A) and CH_4 selectivity (B) for Ni-Zn-Al LDHd, Ni-Zn-Al LDHd + MMT (2:1) and Ni-Zn-Al LDHd + MMT-CTAB (2:1) catalysts tested in Photothermo-catalytic (PT) CO_2 methanation reaction at atmospheric pressure and temperature of 350 °C.

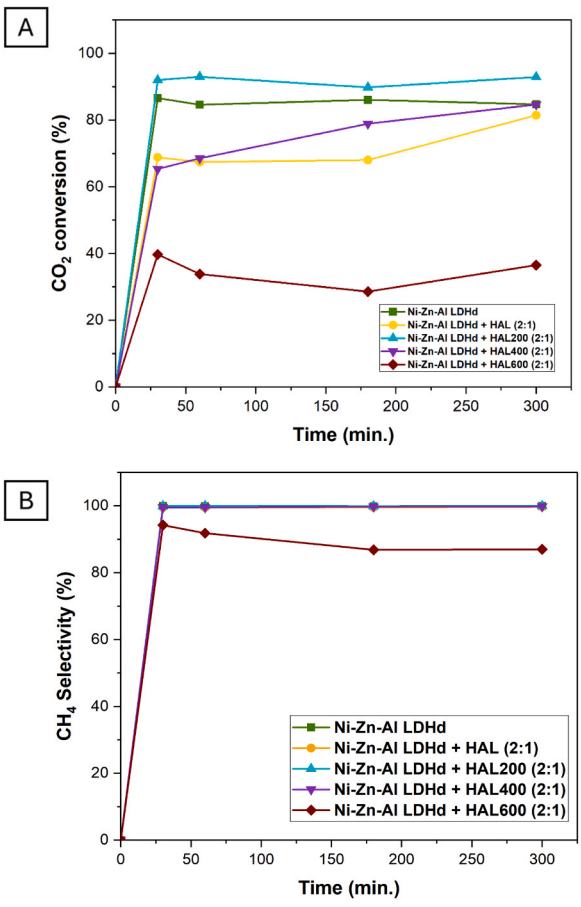

Fig. 3. CO_2 conversion (A) and CH_4 selectivity (B) for Ni-Zn-Al LDHd, Ni-Zn-Al LDHd + HAL (2:1), Ni-Zn-Al LDHd + HAL200 (2:1), Ni-Zn-Al LDHd + HAL400 (2:1) and Ni-Zn-Al LDHd + HAL600 (2:1) catalysts tested in Photothermo-catalytic (PT) CO_2 methanation reaction at atmospheric pressure and temperature of 350 °C.

performance of the bare Ni-Zn-Al LDHd (86 %). The samples containing the halloysite pretreated at 600 °C showed the worst performances reaching a conversion of 40 % and a CH_4 selectivity of 95 % that decrease to 85 % after 5 h of run. The poor activity of this sample can be due to the collapse of the halloysite structure at the high pretreatment temperature [28].

To evaluate the photo-thermal response of the catalysts, the temperatures reached under illumination were measured using an infrared thermal camera. The performance of the Ni-Zn-Al LDHd + HAL200 (2:1) catalyst was compared with that of the bare Ni-Zn-Al LDHd, also considering the heating contribution of the empty reactor (solar lamp effect) (Table S1, Figure S3). For each test, the solar lamp was positioned 10 cm from the reactor.

Table S1 reports the temperatures of the empty reactor and of the reactor loaded with the two catalysts after 3 h (temperature stabilization) of simulated solar irradiation without external heating. Both catalysts exhibited an increase in temperature compared to the empty reactor (ΔT). Specifically, the Ni-Zn-Al LDHd catalyst showed a ΔT of 18.9 °C, while the Ni-Zn-Al LDHd + HAL200 (2:1) sample exhibited a more pronounced temperature rise of 28.8 °C. These results indicate that the addition of halloysite led to an enhanced photo-thermal response of the LDHd catalyst, which may contribute to the higher photothermo-catalytic activity observed for the Ni-Zn-Al LDHd + HAL200 (2:1) sample. However, the influence of this effect will be further investigated in future studies by evaluating the role of reactor geometry and the effective catalyst surface area exposed to irradiation. Indeed, the development of a more efficient photo-thermal response is crucial to exploit other photothermo-catalytic mechanisms as the photo-driven thermocatalysis, in which the thermal energy required to activate the reaction derives from the full conversion of the incident light without external heating.

3.4. Photothermo-catalytic stability tests

The most performing catalysts for each type of composites were tested for 20 h in order to evaluate their stability during the photothermo-catalytic CO_2 methanation (Fig. 4A and B). The three samples tested were: Ni-Zn-Al LDHd (green line), Ni-Zn-Al LDHd + MMT-CTAB (2:1) (yellow line) and Ni-Zn-Al LDHd + HAL200 (2:1) (cyan line). Each catalyst presented a good stability in terms of CO_2 conversion and CH_4 selectivity, except for the Ni-Zn-Al LDHd + MMT-CTAB (2:1) which showed a decrease in CH_4 selectivity during the test, moving from 98 % to 79 % after 20 h. The observed behaviour for the Ni-Zn-Al LDHd + MMT-CTAB (2:1) catalyst, characterized by a progressive shift of selectivity from CH_4 to CO during the stability test, was probably due to the different surface composition of this sample [43] (see also XPS analysis, paragraph 3.6).

3.5. XRD characterization

The XRD patterns of the Ni-Zn-Al LDHd catalyst before and after calcination and reduction are reported in Figures S4A and S4B. It is possible to observe that before the calcination process (Figure S4A) the Ni-Zn-Al LDH presented all the typical signals of hydrotalcites at 2θ = 11.74°, 23.5°, 35.1°, 39.5°, 60.8°, 62.2° (ICSD reference #81963). After the calcination and reduction processes at 600 °C, all these signals disappear and they are replaced by typical signals of metallic Ni at 2θ = 44.5°, 51.6° and 75.5° (ICSD reference #52265) and NiO at 2θ= 37.1°, 65.5° (ICSD reference #87108). There are also some signals attributable to $NiAlO_4$ and $ZnAl_2O_4$ spinel phases at 2θ = 36.5°, 37°, 44.8°, 45.1°, 65.6° and 77.3° (ICSD reference #11261 and #73682). The signals at 37.1°, 44.8° are also attributable at metallic Zn (ICSD reference #247147). From the observed results it is possible to confirm the formation of the LDH structure and its subsequent conversion into a mixed oxide of Ni, Zn and Al. Furthermore, the reduction process allowed the formation of metallic Ni nanoparticles. To confirm the

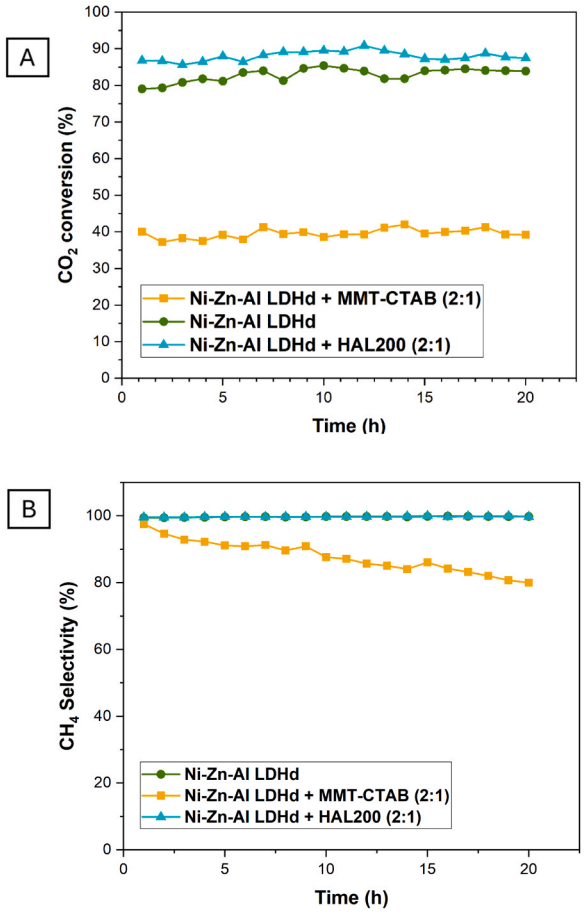

Fig. 4. CO_2 conversion (A) and CH_4 selectivity (B) for Ni-Zn-Al LDHd, Ni-Zn-Al LDHd + HAL200 (2:1) and Ni-Zn-Al LDHd + MMT-CTAB (2:1) catalysts tested in Photothermo-catalytic (PT) CO_2 methanation reaction at atmospheric pressure and temperature of 350 °C for 20 h (stability test).

effectiveness of the reduction process, the XRD analysis was also conducted on the Ni-Zn-Al + HAL200 (2:1) catalyst (the best performing sample) before and after the reduction at 600 °C in a hydrogen flow. The XRD pattern is shown in Figure S4B. For the unreduced sample, only the characteristic reflections of NiO are detected at 2θ = 37.1°, 43.6°, and 65.5°. Following reduction, these reflections markedly decrease in intensity and are replaced by the diffraction signals of metallic Ni at 2θ = 44.5°, 51.6°, and 76.5°

Finally, in Fig. 5, the XRD patterns of Ni-Zn-Al LDHd, Ni-Zn-Al LDHd + HAL200 (2:1) before and after the catalytic test and Ni-Zn-Al LDHd + MMT-CTAB (2:1) are reported. The sample Ni-Zn-Al LDHd + HAL200 (2:1) does not show any structural changes before and after the photothermo-catalytic test thereby confirming the structural stability of the catalyst.

In the Ni-Zn-Al LDHd + MMT-CTAB (2:1) and Ni-Zn-Al LDHd + HAL200 (2:1) all the signals observed in the Ni-Zn-Al LDHd are present, with two additional features at 2θ = 19.05° and 26.75° that can be attributed to quartz (SiO_2) (ICSD reference #16331) likely due to the partial decomposition of the montmorillonite/halloysite [44,45].

3.6. SEM-EDX and XPS analysis

The SEM-EDX analysis was carried out on the samples Ni-Zn-Al LDHd, Ni-Zn-Al LDHd + MMT-CTAB (2:1) and Ni-Zn-Al LDHd + HAL200 (2:1). The halloysite-modified sample pre-treated at 200 °C (Ni-Zn-Al LDHd + HAL200) was also investigated after the photothermo-catalytic test. Fig. 6a shows the SEM micrographs of the

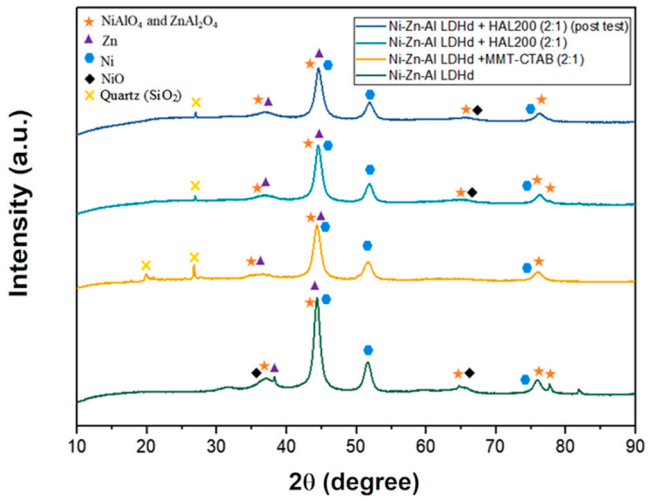

Fig. 5. XRD patterns of the examined samples.

Ni-Zn-Al LDHd sample, which exhibits the typical coral-like shape [13]. The corresponding EDX elemental mapping confirms the homogeneous distribution of the metals (Fig. 6b-c), especially of Ni, and yields a (Ni+Zn)/Al ratio of ~2,5, in good agreement with the nominal value (3) (Table 1).

The SEM images, EDX spectrum, and elemental mapping of the Ni-Zn-Al LDHd+HAL200 sample are reported in Fig. 7. Additional SEM images (Figure S5) highlight the successful addition of halloysite nanotubes into the LDH structure. As reported, the peculiar resultant morphology of the Ni-based LDH derived catalyst supported on halloysite can affect the CO_2 adsorption process [28], therefore the presence of the halloysite nanotubes can be another reason for the higher photothermo-catalytic performance of this sample compared to the other ones.

The EDX analysis (Fig. 7b-c) further demonstrates the uniform distribution of the metallic species and the formation of the LDHd–halloysite composite, as evidenced by the Si signal. As reported in Table 2, the atomic concentrations of Ni and Zn in the Ni-Zn-Al LDHd+HAL200 (2:1) sample are lower than those in the pristine LDH (Table 1), consistent with the nominal composition (see Section 2.1). In this case, the (Ni+Zn)/Al ratio is ~2 (Table 2), which matches the expected value when considering the additional Al contribution from halloysite. Similar considerations can be applied to the Ni-Zn-Al LDHd + MMT-CTAB (2:1) sample, whose SEM-EDX data are reported in Figure S6 and Table S2. The morphology is comparable to the other materials but appears slightly less uniform. Finally, no significant morphological or compositional changes were detected in the spent Ni-Zn-Al LDHd+HAL200 (2:1) sample after the photothermo-catalytic test (Figure S7, Table S3). However, an increased carbon content was observed, likely due to the adsorption of carbonaceous species during the CO_2 methanation reaction.

The XP spectra in the Al 2p region are shown in Fig. 8. The Ni-Zn-Al LDHd, Ni-Zn-Al LDHd + HAL200 (2:1) and Ni-Zn-Al LDHd + HAL200 (2:1) post photothermo-catalytic test samples show XPS broad peaks centered at 74.5 eV, typical of Al_2O_3 species [46]. The XPS of the Ni-Zn-Al LDHd + MMT-CTAB (2:1) sample showed a larger FWHM and was deconvoluted with two Gaussian components at 74.5 eV, due to the Al_2O_3 species, and at 76.1 eV due to the presence of some $Al(OH)_3$, (relative intensity 69 % and 31 %, respectively) [13,46]. The different surface aluminum species observed for the Ni-Zn-Al LDHd + MMT-CTAB (2:1) catalyst could be one of the reasons behind the poor catalytic activity shown by this catalyst, affecting negatively the interaction between the MMT and the LDHd.

Fig. 9 shows the XP spectra in the Zn 2p binding energy region for all the samples. They consist of the Zn $2p_{3/2,1/2}$ spin-orbit components at

Table 1
Atomic concentration (%) from EDX analysis of Ni-Zn-Al LDHd sample.

Element Symbol	Atomic Conc. (%)	$\frac{Ni+Zn}{Al}$
Ni	27.30	2.48
O	49.46	
Zn	8.72	
Al	14.52	

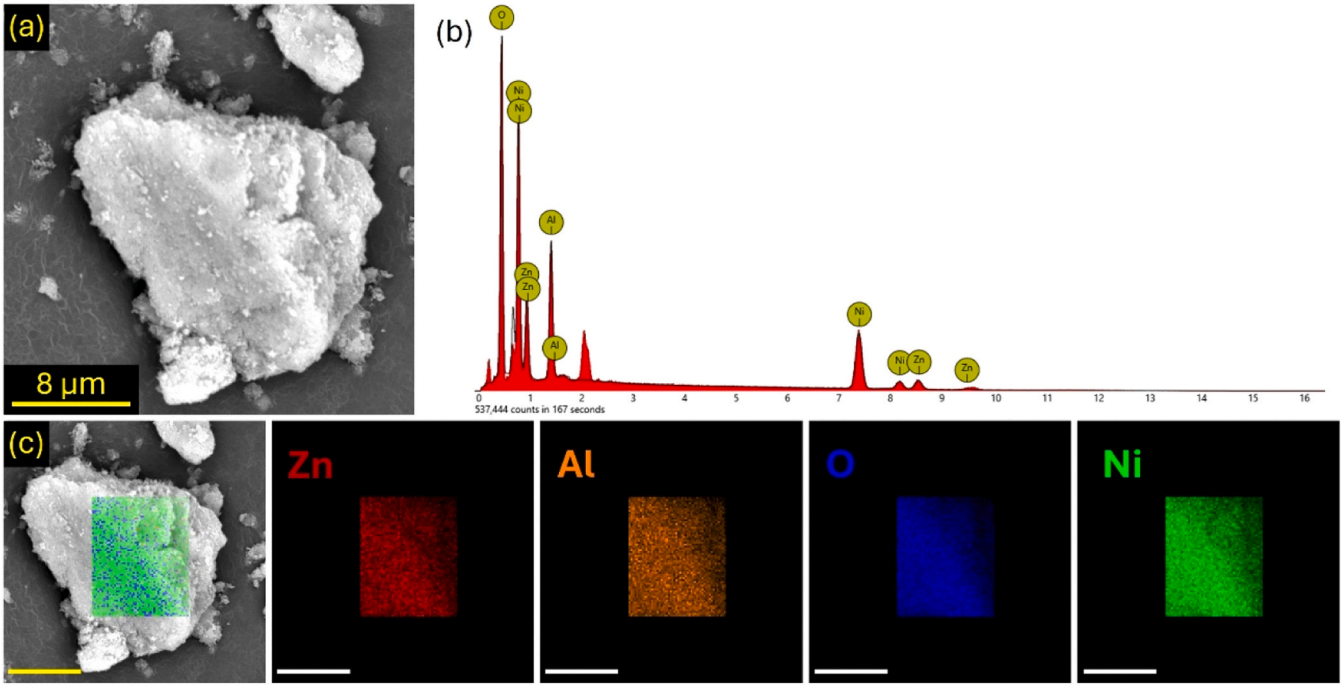

Fig. 6. SEM image (a), EDX spectrum (b) and elemental mapping (c) of Ni-Zn-Al LDHd sample (scale bar 8 μm).

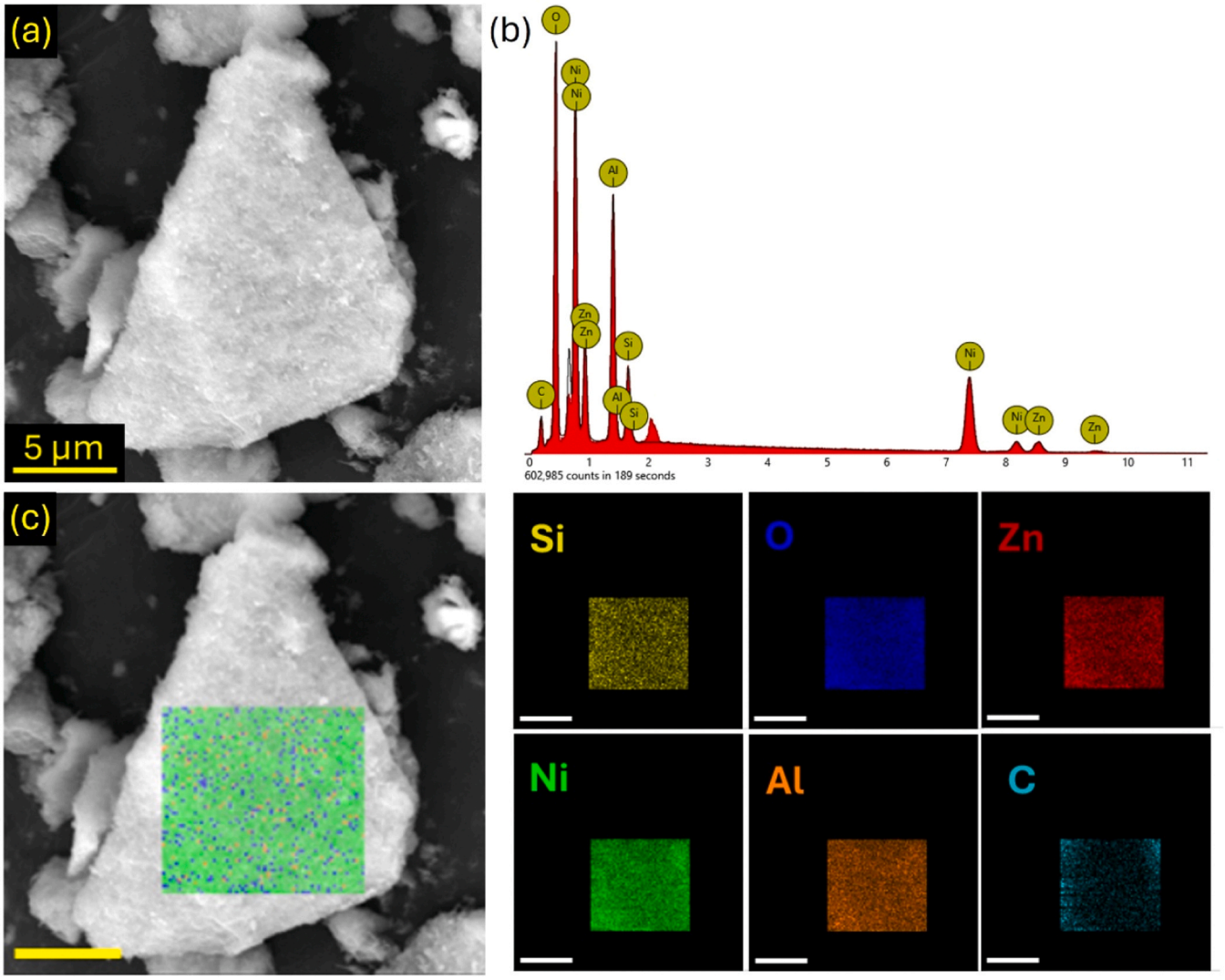

Fig. 7. SEM image (a), EDX spectrum (b) and elemental mapping (c) of Ni-Zn-Al LDHd + HAL200 (2:1) sample (scale bar 5 μm).

Table 2
Atomic concentration from EDX analysis of Ni-Zn-Al LDHd + HAL200 (2:1) sample.

Element	Atomic Conc. (%)	$\frac{Ni+Zn}{Al}$
Ni	18.56	2.04
O	41.94	
Al	12.37	
Zn	6.69	
C	16.76	
Si	3.68	

1021.9 and 1044.9 eV for samples a) Ni-Zn-Al LDHd + HAL200 (2:1), b) Ni-Zn-Al LDHd + HAL200 (2:1) post-test and c) Ni-Zn-Al LDHd due to Zn^0 states [47]. The XPS of the sample d) Ni-Zn-Al LDHd + MMT-CTAB (2:1) shows two Zn $2p_{3/2,1/2}$, spin-orbit doublets at 1021.9–1044.9 and 1022.9–1045.9 eV due to Zn^0 and ZnO levels, respectively (relative intensities 60 and 40 %, respectively) [48].

Fig. 10 shows the XP spectra in the Ni 2p binding energy region for all the samples. They consist of the spin-orbit components of Ni $2p_{3/2,1/2}$ at 855.8 and 873.5 eV. A careful deconvolution of the experimental Ni $2p_{3/2}$ spin-orbit component required three Gaussians at: 852.5–852.8 eV due to the Ni^0 states, 854.6–855.1 eV due to the Ni^{2+} states, and 856.4–856.8 due to the Ni^{3+} levels, for all samples [49,50]. The broad band at 861.4–861.7 eV is due to multiplet contributions in Ni oxides by satellite structures [49].

A comparison of the relative intensities of the Gaussian components for Ni-Zn-Al LDHd + HAL200 (2:1) and for the same sample after the photothermo-catalytic CO_2 methanation test suggests a partial reduction of some Ni^{3+} to Ni^{2+} after the reaction. This behaviour can be attributed both to the reducing environment of the reaction, due to the presence of hydrogen, and to the high temperature, Ni^{3+} tends, in fact, to transform easily into a more stable divalent state at a temperature exceeding 138 °C [51–53]. The presence of Ni^{3+} in the examined samples is typical of ternary or quaternary systems, particularly deriving from LDH precursors [52,54]. In fact, Ni^{3+} is typically considered unstable and tends to rapidly reduce into Ni^{2+}, however the presence of other metals such as Al, Zn or Co in a matrix of mixed oxides determines a stabilization of Ni^{3+}, forming spinel phases such as $NiAlO_4$ (as also detected by XRD), $NiAl_2O_4$, $NiCo_2O_4$ and others [52,55].

The XP spectra for all the samples in the O 1 s binding energy region (Figures S8 a-d) show a single symmetric peak at 531.3 eV, typical of metal oxide states [56].

Figures S9 (a-c) show the XP spectra in the Si 2p binding energy region for the samples Ni-Zn-Al LDHd+ HAL200 (2:1), Ni-Zn-Al LDHd + HAL200 (2:1) post-test and Ni-Zn-Al LDHd + MMT-CTAB (2:1). Apart from a small feature at about 100 eV, due to Si substrate on which the sample powders were deposited, in all cases there is evidence of a broad

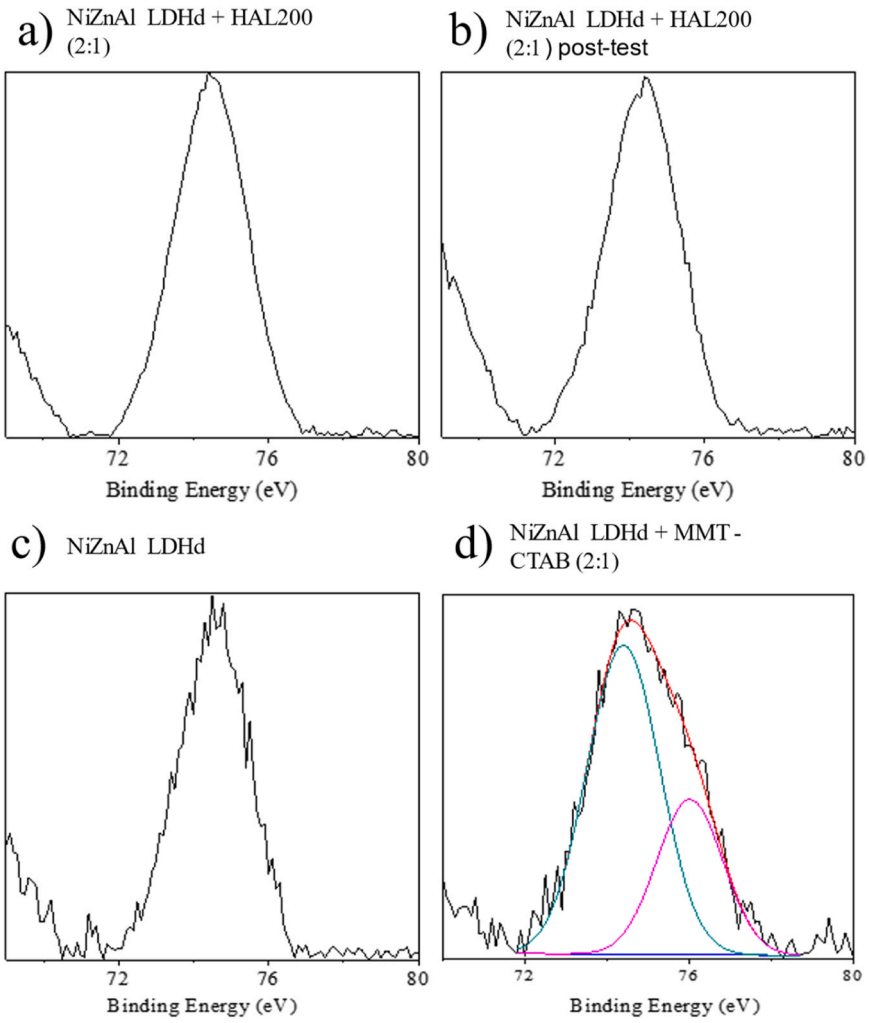

Fig. 8. Al Kα excited XPS in the Al 2p binding energy region for a) Ni-Zn-Al LDHd + HAL200 (2:1); b) Ni-Zn-Al LDHd + HAL200 (2:1) post-test; c) Ni-Zn-Al LDHd; d) Ni-Zn-Al LDHd + MMT-CTAB (2:1). For the latter sample: dark cyan, and magenta lines refer to the 74.5 and 76.1 eV Gaussians components, respectively. The blue line represents the background and the red line superimposed on the experimental black profile refers to the sum of the Gaussian components.

peak at 102.4 eV consistent with the Si 2p levels of SiO_2 species [57,58] attributable to the presence of the phyllosilicates in accordance with XRD and EDX analysis.

In Table 3 the relative surface atomic concentration analysis is reported for all the examined samples. Comparing these data with the results of the EDX analysis (Tables 1, 2, S2 and S3) it is possible to note that the Ni was present in high amount in the less superficial layers of the materials, indeed the Ni XPS surface atomic concentration of the examined samples was always lower compared to the EDX analysis, while it was verified a Zn surface segregation (see Tables 1–3). Furthermore, the amount of Ni on the catalyst surface decreases in favour of Zn upon the addition of halloysite, and this effect becomes particularly pronounced in the presence of montmorillonite. Indeed, the Ni:Zn surface ratio was 1.1 in the Ni-Zn-Al LDHd sample, it decreased to 0.7 in the Ni-Zn-Al LDHd+ HAL200 (2:1) catalyst and was 0.1 in the Ni-Zn-Al LDHd + MMT-CTAB (2:1) sample, pointing to as the addition of phyllosilicates favours the Zn surface segregation. The very low presence of surface Ni in the Ni-Zn-Al LDHd + MMT-CTAB (2:1) catalyst and the higher surface content of Al and Si (Table 3) is a further indication for the drop in the photothermo-catalytic activity observed for this sample, with the MMT that covered the Ni surface active sites. On the contrary, the addition of the modified halloysite promoted the optimal Ni:Zn surface ratio necessary to boost up the CO_2 methanation reaction. Consequently, the $\frac{Ni+Zn}{Al}$ surface ratios were slightly lower compared to those observed with EDX analysis. However, also from the surface concentrations analysis, it is possible to highlight that the Ni+Zn concentration of the best performing catalyst (i.e. the Ni-Zn-Al LDHd+ HAL200 (2:1)) is about 2/3 lower (similar to the nominal one) compared to the Ni+Zn surface concentration of the bare Ni-Zn-Al LDHd (Table 3), highlighting as the strong interaction between the LDHd and the modified halloysite increased the photothermo-catalytic activity with the optimal Ni:Zn surface and bulk distribution, despite the lower metals content compared to the unmodified Ni-Zn-Al LDHd sample.

3.7. *Textural and optical properties*

The textural properties of the synthesized samples were investigated through N_2 physisorption. The isotherms were collected for the Ni-Zn-Al LDHd, Ni-Zn-Al LDHd + HAL200 (2:1) and the Ni-Zn-Al LDHd + MMT-CTAB (2:1) samples and are shown in Figure S10a. All the samples showed a type V isotherm which is typical of relatively weak adsorbent–adsorbate interactions; the hysteresis loops are of H1 type for each sample, suggesting the presence of uniform mesopores [59]. The surface area values, obtained by the application of BET method, are shown in Table 4. The pore distribution (Figure S10b) was also obtained by the application of the BJH method, the mean pore diameter and pore volume values calculated for each sample are also reported in Table 4. The modification of the LDHd by the addition of MMT-CTAB and HAL200 led

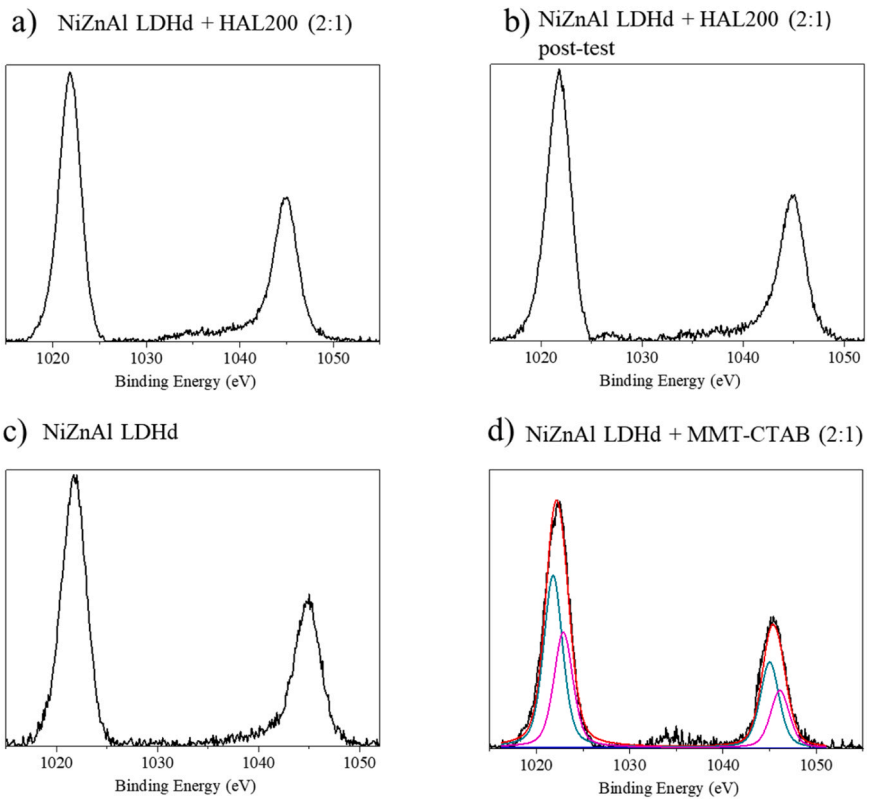

Fig. 9. Al Kα excited XPS in the Zn 2p binding energy region: a) Ni-Zn-Al LDHd + HAL200 (2:1); b) Ni-Zn-Al LDHd + HAL200 (2:1) post-test; c) Ni-Zn-Al LDHd; d) Ni-Zn-Al LDHd + MMT-CTAB (2:1). For the latter sample: dark cyan, and magenta lines refer to 1021.9–1044.9 and 1022.9–1045.9 eV Gaussians components, respectively. The blue line represents the background and the red line superimposed on the experimental black profile refers to the sum of the Gaussian components.

to an increase in the surface area and a decrease in the mean pore diameter and volume. The mean pore diameter values confirmed the mesoporous nature of the materials according to the observed isotherms. Interestingly, the Ni-Zn-Al LDHd + HAL200 (2:1) showed the highest surface area and the lowest mean pore diameter and these features can positively affect the photothermo-catalytic CO_2 conversion, due to the presence of a large number of active sites for the CO_2 adsorption/activation. Indeed, this sample was the most active one (Fig. 3).

The UV-Vis DRS characterization was performed on the same samples; the value of the optical bandgap (Eg) was calculated by the application of the Kubelka-Munk function. The reflectance spectra for all the samples and the Kubelka-Munk spectrum of the Ni-Zn-Al LDHd + HAL200 (2:1) are reported in Figures S11 a-c and S12 respectively, the optical band-gap values are reported in the Table 4. All the samples showed similar optical properties with a decrease in reflectance in the range 250–350 nm (Figures S11 a-c), with a feature in the visible region (450–600 nm) typical of the hydrotalcites-derived catalysts [13]. The addition of HAL200 and MMT-CTAB modified the optical band-gap of the material leading to a decrease in the Eg value compared to Ni-Zn-Al LDHd sample. Although the Ni-Zn-Al LDHd + MMT-CTAB (2:1) showed the lowest Eg, it was also the worst photothermo-catalyst for the CO_2 methanation compared to Ni-Zn-Al LDHd and Ni-Zn-Al LDHd + HAL200 (2:1) (Fig. 4). This highlights, as in this case, the Eg is not a crucial parameter to favour the photothermo-catalytic conversion of CO_2.

3.8. CO_2-TPD

The CO_2-TPD profiles of the Ni-Zn-Al LDHd, Ni-Zn-Al LDHd + HAL200 (2:1) and Ni-Zn-Al LDHd + MMT-CTAB (2:1) samples are shown in Fig. 11. The three zones indicated as α, β and γ, are related to the presence of weak, medium and strong basic sites, respectively [60]. For the efficient conversion of CO_2 to methane, the basicity of the active sites must be carefully balanced. Sites that adsorb CO_2 too weakly fail to activate the molecule, while excessively strong adsorption hinders its mobility and subsequent conversion of CO_2, due to the difficulty in the activation of the chemisorbed molecules. Therefore the presence of medium basic sites is required to favour the CO_2 conversion reaction [13,61].

All the samples exhibited a low-temperature desorption peak (α) within the 58–70 °C range, which is attributed to the interaction between surface hydroxyl groups and weakly adsorbed CO_2 species [13,62]. Also, all samples showed peaks in the temperature ranges of 114–123 °C (α), 148–156 °C (β), 175–177 °C (β) and 200–203 °C (β) but only the Ni-Zn-Al LDHd + HAL200 (2:1) showed a fifth peak at 221,5 °C (β). All peaks in the β zone are attributable to the presence of medium strength basic sites in particular to the desorption of CO_2 from metal–oxygen pairs (M^{n+}–O^{2-} sites) [13,62].

The quantitative analysis of basic sites is reported in Table 5. The distribution of basic sites in the three samples showed significant differences both in terms of sites strength and in the total amount of basic sites (TA_{BS}). The Ni-Zn-Al LDH_d sample exhibited a high total basicity (1.27 mmol·g^{-1}) and a strong predominance of weak sites (80.3 %). The addition of halloysite pretreated at 200 °C in the Ni-Zn-Al LDHd + HAL200 (2:1) composite resulted in a slight decrease in total basicity (1.14 mmol·g^{-1}), but it is possible to note an increase in medium sites (27.3 %) compared to the Ni-Zn-Al LDHd (19.7 %). This confirms that the interaction between the LDHd and halloysite modifies the distribution of basic sites, increasing the medium basic sites, ideal to favour an efficient CO_2 activation. In the case of the Ni-Zn-Al LDHd + MMT-CTAB (2:1) composite, the lowest total basicity was observed (0.84 mmol g^{-1}), with a distribution strongly shifted toward weak sites (84.7 %). The reduced content of medium sites indicates that the incorporation of montmorillonite attenuates the strength of surface basic sites, likely due to the partial coverage of the LDH_d layers by montmorillonite. The Ni-

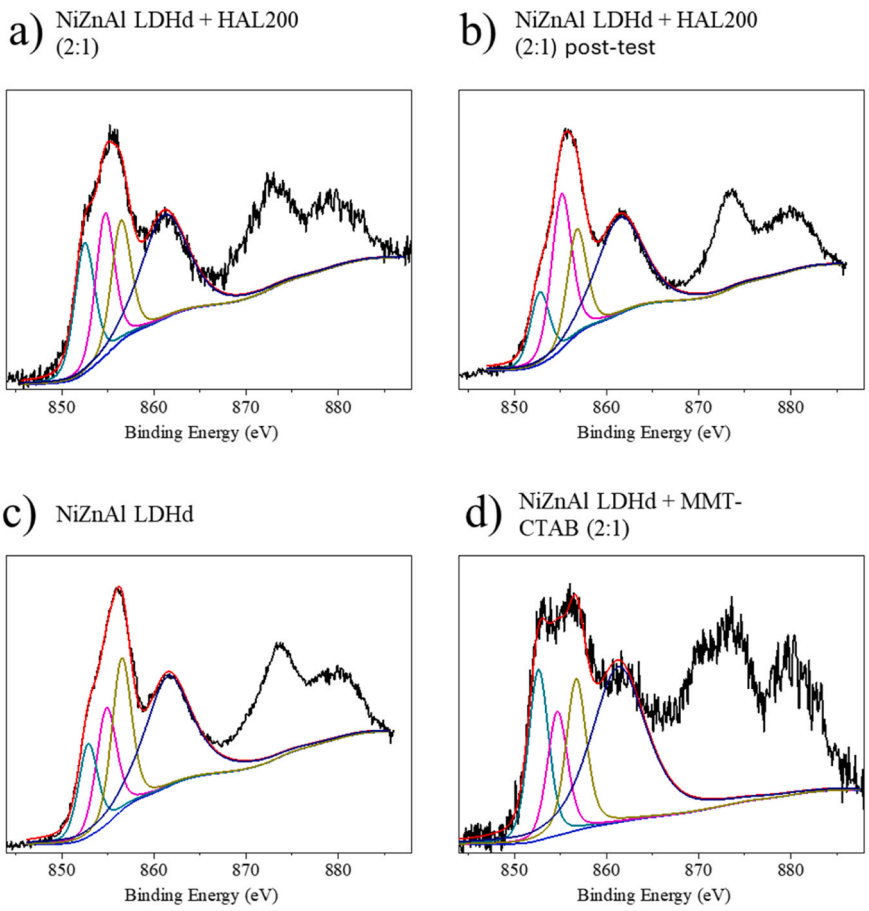

Fig. 10. Al Kα excited XPS in the Ni 2p binding energy region: a) Ni-Zn-Al LDHd + HAL200 (2:1); b) Ni-Zn-Al LDHd + HAL200 (2:1) post-test; c) Ni-Zn-Al LDHd; d) Ni-Zn-Al LDHd + MMT-CTAB (2:1). Dark cyan, magenta, dark yellow, and navy lines refer to the Gaussians components, respectively. The blue line represents the background and the red line superimposed on the experimental black profile refers to the sum of the Gaussian components.

Table 3
XPS relative atomic concentration (%) analysis for the examined samples*.

Samples	O 1 s (%)	Ni 2p (%)	Zn 2p (%)	Al 2p (%)	Si 2p (%)	$\frac{Ni+Zn}{Al}$
Ni-Zn-Al LDHd + HAL200 (2:1)	69.5	6.8	9.6	10.0	4.1	1.64
Ni-Zn-Al LDHd + HAL200 (2:1) post-test	69.3	7.6	10.3	9.2	3.6	1.94
Ni-Zn-Al LDHd	59.5	14.1	12.3	13.0	1.1	2.03
Ni-Zn-Al LDHd + MMT-CTAB (2:1)	20.2	3.5	28.9	27.4	20.0	1.18

*The observed Si content can be affected by the use of a Si substrate to carry out the XPS analysis. In the case of the Ni-Zn-Al LDHd the Si content is due exclusively to the presence of this sample preparation substrate.

Table 4
Textural and optical features of synthesized samples.

Samples	BET surface area (m^2/g)	Mean pore diameter (nm)	Pore volume (cm^3/g)	Optical band gap (eV)
Ni-Zn-Al LDHd	105.7	24	0.63	3.43
Ni-Zn-Al LDHd + HAL200 (2:1)	127.1	7.2	0.29	3.14
Ni-Zn-Al LDHd + MMT-CTAB (2:1)	111.7	11.1	0.44	2.85

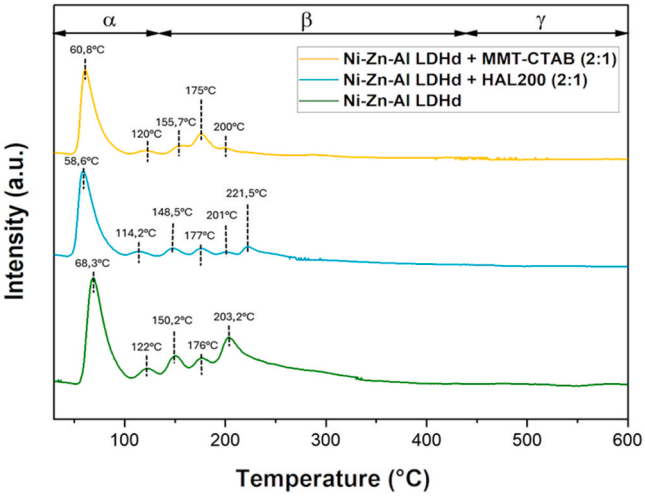

Fig. 11. CO_2-TPD profiles of the examined samples.

ZnAl + HAL200 (2:1) catalyst, with the highest distribution of medium basic sites (Table 5) and the highest surface area (Table 4), favours CO_2 adsorption and activation, thereby enhancing photothermo-catalytic CH_4 production.

Table 5
Quantitative analysis of basic sites. α: weak (T < 140 °C); β: medium (140 °C<T < 450 °C); γ: strong (T > 450 °C) basic sites; TA_{BS}: total amount of basic sites in mmol $CO_2 \bullet g_{cat}^{-1}$.

Sample	Basic sites			
	α (%)	β (%)	γ (%)	TA_{BS}
Ni-Zn-Al LDHd	80.3 %	19.7 %	/	1.27
Ni-Zn-Al LDHd + HAL200 (2:1)	72.7 %	27.3 %	/	1.14
Ni-Zn-Al LDHd + MMT-CTAB (2:1)	84.7 %	15.3 %	/	0.84

4. Discussion

The CO_2 methanation reaction was efficiently promoted by a photothermo co-catalytic mechanism on the Ni-Zn-Al LDHd sample. The addition of halloysite treated at 200 °C increases the surface area, promotes the formation of additional medium-strength basic sites and favours a decrease in the optical band gap compared to the Ni-Zn-Al LDHd. As a consequence of these changes, an increase in activity for the Ni-Zn-Al LDHd + HAL200 (2:1) catalyst was observed, reaching CO_2 conversion up to 92 % and selectivity to CH_4 > 99 %, despite the lower Ni content (Fig. 3). The incorporation of montmorillonite, instead, led to a significant lower activity compared to the bare Ni-Zn-Al LDHd sample. In addition, the Ni-Zn-Al LDHd + MMT-CTAB (2:1) catalyst showed lower stability than the other samples, showing a variation of selectivity in methane that during the stability tests fell from 98 % to 79 %, favouring the production of CO (Fig. 4). This behaviour can be explained on the basis of the different surface composition of this sample with the MMT that covered the Ni surface active sites, as verified by XPS. Indeed, one of the reaction mechanisms proposed for CO_2 methanation on catalysts containing Ni supported on basic oxides [63,64] suggests that after the adsorption of CO_2 on the basic sites of the support and the adsorption and splitting of H_2 on the metallic sites of the catalyst, a common fundamental step, both for the production of CH_4 and CO, is the formation of the formate intermediate, HCOO* and the subsequently conversion in CO*. As suggested by *Wang et al.* [43], only the medium-strength basic sites allow an efficient hydrogenation of the CO*intermediate to methane. The low amount of these medium-strength basic sites or of a very low concentration of Ni metallic sites, as in the Ni-Zn-Al LDHd + MMT-CTAB (2:1) catalyst, favours the CO_2 adsorption on weak basic sites promoting the desorption of CO*, with formation of gaseous CO, instead of being converted into methane. Moreover, the markedly lower surface concentration of Ni observed for the Ni-Zn-Al LDHd + MMT-CTAB (2:1) sample (Table 3) and the limited availability of surface Ni sites hinders effective H_2 activation, which is essential for the CO_2 methanation process.

On the contrary, the addition of the modified halloysite on the Ni-Zn-Al LDHd promoted the optimal Ni:Zn surface ratio with a Zn surface segregation that is essential to exploit the photocatalytic features of the Zn species (as the $ZnAl_2O_4$, detected by XRD), allowing to have a synergistic beneficial effect with the thermocatalytic properties activated by the Ni species (NiO, $NiAlO_4$, as confirmed by XRD) [13,65]. Moreover, the presence of halloysite endorsed an efficient CO_2 adsorption and activation in the medium-strength basic sites, leading to have holistic effects that boosted up the photothermo-catalytic CO_2 conversion despite the lower content of metal active species compared to the unmodified Ni-Zn-Al LDHd sample. This is a fascinating strategy to guarantee good catalytic performance with a high sustainability and efficient use of the resources and of the raw materials.

5. Conclusions

This study demonstrates the potential of phyllosilicates-modified Ni-Zn-Al Layered Double Hydroxide-derived catalysts for efficient photothermo-catalytic CO_2 methanation under mild conditions. The unmodified Ni-Zn-Al LDHd catalyst exhibited excellent performance, achieving high CO_2 conversion (86 %) and CH_4 selectivity (>99 %), through a mechanism of photo-thermo co-catalysis. Among the phyllosilicate-modified materials, only the incorporation of halloysite pre-treated at 200 °C (Ni-Zn-Al LDHd + HAL200 (2:1)) resulted in a further enhancement of photothermo-catalytic performance, with CO_2 conversion reaching up to 92 %, despite a lower Ni content. This improvement is attributed to the highest surface area, the presence of additional medium-strength basic sites and the reduced optical band gap. In contrast, the use of montmorillonite, even after CTAB intercalation, led to a decrease in activity and stability, related to the very low concentration of surface Ni and the different surface composition.

Stability tests, carried out in the photothermo-catalytic approach for 20 h, confirmed the stability and the consistent performance of the Ni-Zn-Al LDHd + HAL200 (2:1) catalyst over continuous heating at 350 °C under simulated solar irradiation. The XPS and SEM-EDX characterization proved that no significant variations in the structure, composition and morphology of the Ni-Zn-Al LDHd + HAL200 (2:1) occurred during the photothermo- catalytic tests.

These findings highlight that the catalytic properties of LDH-derived systems can be finely tuned by the interaction with appropriate phyllosilicates, leading to enhanced catalytic performances with a low metals content. In particular, halloysite-based composites emerged as promising materials for developing low-metal-content sustainable catalysts for efficient solarphoto-thermo co-catalytic CO_2 methanation. In future works, more efforts should be made on a deep investigation on the morphology and size of Ni particles with an advanced and deep morphological characterization by HR-TEM or STEM, correlating the morphological Ni properties to the peculiar phyllosilicate added on the LDH-derived catalyst. Specifically, due to the promising performance of halloysite, we will test similar phyllosilicates such as the kaolinite.

CRediT authorship contribution statement

Luca Calantropo: Writing – review & editing, Writing – original draft, Investigation, Formal analysis, Data curation, Conceptualization. **Eleonora La Greca:** Investigation, Data curation. **Leonarda Francesca Liotta:** Writing – review & editing, Visualization, Validation, Funding acquisition, Resources. **Giuliana Impellizzeri:** Resources, Investigation. **Antonino Gulino:** Investigation, Data curation. **Angelo Ferlazzo:** Investigation, Data curation. **Libera Vitiello:** Investigation, Formal analysis, Data curation. **Sabrina Carola Carroccio:** Writing – review & editing, Resources, Funding acquisition. **Salvatore Scirè:** Writing – review & editing, Resources. **Roberto Fiorenza:** Writing – review & editing, Validation, Supervision, Investigation, Conceptualization, Writing – original draft,Funding acquisition

Declaration of Competing Interest

The authors declare that they have no known competing financial interests or personal relationships that could have appeared to influence the work reported in this paper.

Acknowledgements

R. Fiorenza thanks for the financial support under the National Recovery and Resilience Plan (NRRP), funded by the European Union – NextGenerationEU—DD 1409 Progetti di Rilevante Interesse Nazionale (PRIN) 2022 PNRR published on 14–09–2022 by the Italia MUR, Missione 4 (Istruzione e Ricerca) Component 2, Investment the CO2@ photothermocat project (P2022JXKKF, CUP E53D23015700001).

L. F. Liotta thanks the project "*Accordo di programma per la regolamentazione dei rapporti in relazione allo svolgimento di attività di ricerca nell'ambito del piano nazionale di ripresa e resilienza (PNRR) - missione 2 "rivoluzione verde e transizione ecologica" – componente 2 "energia rinnovabile, idrogeno, rete e mobilità sostenibile" – investimento 3.5 "ricerca e sviluppo sull'idrogeno*" – AdP ENEA CNR (CUP B93C22000630006).

This research was also partially funded by the European Union (NextGeneration EU) through the MIUR-PNRR project SAMOTHRACE-Sicilian MicronanoTech Research and Innovation Center (ECS00000022, CUP B63C22000620005).

The authors thank the BRIT of the University of Catania for the XPS facilities.

E. La Greca thanks the University of Perugia for the national PhD scholarship in catalysis.

Appendix A. Supporting information

Supplementary data associated with this article can be found in the online version at doi:10.1016/j.jcou.2025.103302.

Data availability

Data will be made available on request.

References

[1] Q.A. Nwabueze, S. Leggett, Advancements in the Application of CO_2 Capture and Utilization Technologies-A Comprehensive Review, (2024) 508–532. ⟨www.preprints.org⟩.

[2] Z. Turakulov, A. Kamolov, A. Norkobilov, M. Variny, G. Díaz-Sainz, L. Gómez-Coma, M. Fallanza, Assessing various CO_2 utilization technologies: a brief comparative review, J. Chem. Technol. Biotechnol. 99 (2024) 1291–1307, https://doi.org/10.1002/jctb.7606.

[3] X.Y.D. Soo, J.J.C. Lee, W.Y. Wu, L. Tao, C. Wang, Q. Zhu, J. Bu, Advancements in CO_2 capture by absorption and adsorption: a comprehensive review, J. CO_2 Util. 81 (2024) 102727, https://doi.org/10.1016/j.jcou.2024.102727.

[4] C. Kim, C.J. Yoo, H.S. Oh, B.K. Min, U. Lee, Review of carbon dioxide utilization technologies and their potential for industrial application, J. CO_2 Util. 65 (2022) 102239, https://doi.org/10.1016/j.jcou.2022.102239.

[5] IPCC, Section 4: Near-Term Responses in a Changing Climate, Clim. Chang. 2023 Synth. Rep. (2023) 42–66. https://doi.org/10.59327/IPCC/AR6-9789291691647.

[6] F.D. Meylan, V. Moreau, S. Erkman, CO_2 utilization in the perspective of industrial ecology, an overview, J. CO_2 Util. 12 (2015) 101–108, https://doi.org/10.1016/j.jcou.2015.05.003.

[7] O.A. Ojelade, S.F. Zaman, A review on CO_2 hydrogenation to lower olefins: understanding the structure-property relationships in heterogeneous catalytic systems, J. CO_2 Util. 47 (2021) 101506, https://doi.org/10.1016/j.jcou.2021.101506.

[8] Z. Uddin, B.Y. Yu, H.Y. Lee, Evaluation of alternative processes of CO_2 methanation: design, optimization, control, techno-economic and environmental analysis, J. CO_2 Util. 60 (2022) 101974, https://doi.org/10.1016/j.jcou.2022.101974.

[9] T. Yarbaş, N. Ayas, A detailed thermodynamic analysis of CO_2 hydrogenation to produce methane at low pressure, Int. J. Hydrog. Energy 49 (2024) 1134–1144, https://doi.org/10.1016/j.ijhydene.2023.06.223.

[10] S. Escorihuela, C. Cerdá-Moreno, F. Weigelt, S. Remiro-Buenamañana, S. Escolástico, A. Tena, S. Shishatskiy, T. Brinkmann, A. Chica, J.M. Serra, Intensification of catalytic CO_2 methanation mediated by in-situ water removal through a high-temperature polymeric thin-film composite membrane, J. CO_2 Util. 55 (2022) 1–9, https://doi.org/10.1016/j.jcou.2021.101813.

[11] M.A.A. Aziz, A.A. Jalil, S. Triwahyono, M.W.A. Saad, CO_2 methanation over Ni-promoted mesostructured silica nanoparticles: influence of Ni loading and water vapor on activity and response surface methodology studies, Chem. Eng. J. 260 (2015) 757–764, https://doi.org/10.1016/j.cej.2014.09.031.

[12] J. Zhao, Y. Bai, X. Liang, T. Wang, C. Wang, Photothermal catalytic CO_2 hydrogenation over molybdenum carbides: crystal structure and photothermocatalytic synergistic effects, J. CO_2 Util. 49 (2021) 101562, https://doi.org/10.1016/j.jcou.2021.101562.

[13] R. Fiorenza, L. Calantropo, E. La Greca, L.F. Liotta, A. Gulino, A. Ferlazzo, M. G. Musumeci, G. Proietto Salanitri, S.C. Carroccio, G. Dativo, M.T. Armeli Iapichino, S. Scirè, G. Impellizzeri, Solar-promoted photo-thermal CO_2 methanation on SiC/hydrotalcites-derived catalysts, Catal. Today 449 (2025) 115182, https://doi.org/10.1016/j.cattod.2024.115182.

[14] U. Ulmer, T. Dingle, P.N. Duchesne, R.H. Morris, A. Tavasoli, T. Wood, G.A. Ozin, Fundamentals and applications of photocatalytic CO_2 methanation, Nat. Commun. 10 (2019) 1–12, https://doi.org/10.1038/s41467-019-10996-2.

[15] X. Shi, Y. Huang, Y. Bo, D. Duan, Z. Wang, J. Cao, G. Zhu, W. Ho, L. Wang, T. Huang, Y. Xiong, Highly selective photocatalytic CO_2 methanation with water vapor on single-atom platinum-decorated defective carbon nitride, Angew. Chem. 134 (2022) e202203063, https://doi.org/10.1002/ange.202203063.

[16] R. Fiorenza, M. Bellardita, S.A. Balsamo, A. Gulino, M. Condorelli, G. Compagnini, S. Scirè, L. Palmisano, A solar photothermo-catalytic combined process for the VOCs combustion and the subsequent CO_2 valorization using noble metal-free catalysts, Catal. Today 413–415 (2023) 113949, https://doi.org/10.1016/j.cattod.2022.11.010.

[17] T. Rajkumar, A. Sápi, M. Ábel, F. Farkas, J.F. Gómez-Pérez, Á. Kukovecz, Z. Kónya, Ni–Zn–Al-based oxide/spinel nanostructures for high performance, methane-selective CO_2 hydrogenation reactions, Catal. Lett. 150 (2020) 1527–1536, https://doi.org/10.1007/s10562-019-03051-8.

[18] C. Prasad, H. Tang, Q.Q. Liu, S. Zulfiqar, S. Shah, I. Bahadur, An overview of semiconductors/layered double hydroxides composites: properties, synthesis, photocatalytic and photoelectrochemical applications, J. Mol. Liq. 289 (2019) 111114, https://doi.org/10.1016/j.molliq.2019.111114.

[19] Q.L.Tengfei Zhang, Zhiwei Tian, Three-dimensional flower-like nickel phyllosilicates for CO_2 methanation: enhanced catalytic activity and high stability, Sustain. Energy Fuels 4 (2020) 3438–3449, https://doi.org/10.1039/D0SE00360C.

[20] G. Dativo, E. La Greca, L.F. Liotta, V. La Parola, M. Condorelli, G. Impellizzeri, G. Compagnini, S. Scirè, R. Fiorenza, Solar photothermo-catalytic conversion of CO_2 on phyllosilicates modified with Ni and CeO_2, J. CO_2 Util. 82 (2024) 102765, https://doi.org/10.1016/j.jcou.2024.102765.

[21] Y. Zhang, Q. Liu, Nickel phyllosilicate derived Ni / SiO_2 catalysts for CO_2 methanation: identifying effect of silanol group concentration, J. CO_2 Util. 50 (2021) 101587, https://doi.org/10.1016/j.jcou.2021.101587.

[22] T.M. Steeves, A.P. Esser-Kahn, Demonstration of the photothermal catalysis of the Sabatier reaction using nickel nanoparticles and solar spectrum light, RSC Adv. (2021) 8394–8397, https://doi.org/10.1039/d0ra09939b.

[23] Z. Xiao, P. Li, H. Zhang, S. Zhang, Y. Zhao, J. Gu, Journal of colloid and interface science boosting photo-thermal co-catalysis CO_2 methanation by tuning interface electron transfer via Mott-Schottky heterojunction effect, J. Colloid Interface Sci. 672 (2024) 642–653, https://doi.org/10.1016/j.jcis.2024.06.052.

[24] D. dos S. Lima, Y.R. Dias, O.W. Perez-Lopez, CO_2 methanation over Ni–Al and Co–Al LDH-derived catalysts: the role of basicity, Sustain. Energy Fuels 4 (2020) 5747–5756, https://doi.org/10.1039/D0SE01059F.

[25] S. Chen, A.M. Abdel-Mageed, M. Dyballa, M. Parlinska-Wojtan, J. Bansmann, S. Pollastri, L. Olivi, G. Aquilanti, R.J. Behm, Raising the CO_x methanation activity of a Ru/γ-Al_2O_3 catalyst by activated modification of metal–support interactions, Angew. Chem. Int. Ed. 59 (2020) 22763–22770, https://doi.org/10.1002/anie.202007228.

[26] Z. Wang, L. Wang, Y. Cui, Y. Xing, W. Su, Research on nickel-based catalysts for carbon dioxide methanation combined with literature measurement, J. CO_2 Util. 63 (2022) 102117, https://doi.org/10.1016/j.jcou.2022.102117.

[27] S.L. Nie, Y.M. Yan, H.F. Li, L.B. Niu, J.R. Qin, L.G. Chen, G.Y. Bai, A doubly confined nickel-based catalyst derived from hydrotalcite-montmorillonite composite: preparation and hydrogenation performance, ChemCatChem 13 (2021) 2887–2895, https://doi.org/10.1002/cctc.202001256.

[28] J. Wang, Y. Zhang, J. Si, W. Zhang, Q. Liang, W. Li, B. Jin, S. Miao, Structural engineering of NiFe-Layered double hydroxides and halloysite composites for efficient CO_2 capture, Chem. Eng. J. 463 (2023) 142502, https://doi.org/10.1016/j.cej.2023.142502.

[29] P. Makuła, M. Pacia, W. Macyk, How to correctly determine the band gap energy of modified semiconductor photocatalysts based on UV–Vis spectra, J. Phys. Chem. Lett. 9 (2018) 6814–6817, https://doi.org/10.1021/acs.jpclett.8b02892.

[30] D. Briggs, J.T. Grant, In Surface Analysis by Auger and X-Ray Photoelectron Spectroscopy, IM Publications, Chichester, UK, and Surface Spectra Ltd., Manchester, UK, 2003.

[31] A. Gulino, Structural and electronic characterization of self-assembled molecular nanoarchitectures by X-ray photoelectron spectroscopy, Anal. Bioanal. Chem. 405 (2013) 1479–1495, https://doi.org/10.1007/s00216-012-6394-8.

[32] G. Greczynski, L. Hultman, Compromising science by ignorant instrument calibration—need to revisit half a century of published XPS data, Angew. Chem. 132 (2020) 5034–5038, https://doi.org/10.1002/ange.201916000.

[33] R. Fiorenza, C. Contarino, V. Spanò, M.T.A. Iapichino, S.A. Balsamo, Photothermo-catalytic strategies for the CO_2 valorisation using TiO_2-based composites, Catal. Today 423 (2023) 114251, https://doi.org/10.1016/j.cattod.2023.114251.

[34] Y.R. Dias, F. Bernardi, O.W. Perez-Lopez, Improving low-temperature CO_2 methanation by promoting Ni-Al LDH-derived catalysts with alkali metals, ChemCatChem 15 (2023) e202300834, https://doi.org/10.1002/cctc.202300834.

[35] J. Lin, C. Ma, J. Luo, X. Kong, Y. Xu, G. Ma, J. Wang, C. Zhang, Z. Li, M. Ding, Preparation of Ni based mesoporous Al_2O_3 catalyst with enhanced CO_2 methanation performance, RSC Adv. 9 (2019) 8684–8694, https://doi.org/10.1039/c8ra10348h.

[36] L.O. Paulista, A.F.P. Ferreira, B. Castanheira, M.B. Đolić, R.J.E. Martins, R.A. R. Boaventura, V.J.P. Vilar, T.F.C.V. Silva, Solar-driven thermo-photocatalytic CO_2 methanation over a structured RuO_2:TiO_2/SBA-15 nanocomposite at low temperature, Appl. Catal. B Environ. 340 (2024) 123232, https://doi.org/10.1016/j.apcatb.2023.123232.

[37] Y. Chen, Y. Zhang, G. Fan, L. Song, G. Jia, H. Huang, S. Ouyang, J. Ye, Z. Li, Z. Zou, Cooperative catalysis coupling photo-/photothermal effect to drive Sabatier reaction with unprecedented conversion and selectivity, Joule 5 (2021) 3235–3251, https://doi.org/10.1016/j.joule.2021.11.009.

[38] G. Garbarino, P. Riani, L. Magistri, G. Busca, A study of the methanation of carbon dioxide on Ni/Al_2O_3 catalysts at atmospheric pressure, Int. J. Hydrog. Energy 39 (2014) 11557–11565, https://doi.org/10.1016/j.ijhydene.2014.05.111.

[39] L.A. Sani, H. Bai, Z. Xu, L. Fu, Y. Sun, X. Huang, H. Gao, X. Liu, D. Bai, Z. Zhang, F. Su, J. Liu, G. Xu, Optimized combustion temperature in the facile synthesis of Ni/Al_2O_3 catalyst for CO_2 methanation, J. CO_2 Util. 80 (2024) 102678, https://doi.org/10.1016/j.jcou.2024.102678.

[40] G.J. Hutchings, Methanation of carbon dioxide, Appl. Catal. A Gen. 84 (1992) N18, https://doi.org/10.1016/0926-860x(92)80119-w.

[41] R. Ma, J. Sun, D.H. Li, J.J. Wei, Review of synergistic photo-thermo-catalysis: mechanisms, materials and applications, Int. J. Hydrog. Energy 45 (2020) 30288–30324, https://doi.org/10.1016/j.ijhydene.2020.08.127.
[42] D. Mateo, J.L. Cerrillo, S. Durini, J. Gascon, Fundamentals and applications of photo-thermal catalysis, Chem. Soc. Rev. 50 (2021) 2173–2210, https://doi.org/10.1039/d0cs00357c.
[43] X. Wang, H. Shi, J. Szanyi, Controlling selectivities in CO_2 reduction through mechanistic understanding, Nat. Commun. 8 (2017) 1–6, https://doi.org/10.1038/s41467-017-00558-9.
[44] Y. Qin, T. Peng, H. Sun, L. Zeng, Y. Li, C. Zhou, Effect of montmorillonite layer charge on the thermal stability of bentonite, Clays Clay Min. 69 (2021) 328–338, https://doi.org/10.1007/s42860-021-00117-w.
[45] S. Bordeepong, D. Bhongsuwan, T. Pungrassami, T. Bhongsuwan, Characterization of halloysite from thung yai district, Nakhon Si Thammarat Province, in Southern Thailand, Songklanakarin J. Sci. Technol. 33 (2011) 599–607.
[46] D.A. Cristaldi, C.G. Fortuna, A. Gulino, A photoelectron spectroscopy study of lava stones, Anal. Methods 5 (2013) 3458–3462, https://doi.org/10.1039/c3ay40136g.
[47] L. Zhang, J. Yan, M. Zhou, Y. Yang, Y.N. Liu, Fabrication and photocatalytic properties of spheres-in-spheres ZnO/$ZnAl_2O_4$ composite hollow microspheres, Appl. Surf. Sci. 268 (2013) 237–245, https://doi.org/10.1016/j.apsusc.2012.12.069.
[48] A. Gulino, P. Dapporto, P. Rossi, I. Fragalà, Synthesis and characterization of liquid MOCVD precursors for thin films of cadmium oxide, Chem. Mater. 14 (2002) 4955–4962, https://doi.org/10.1021/cm021183m.
[49] V. Iacono, M. Scuderi, M.L. Amoruso, A. Gulino, F. Ruffino, S. Mirabella, Pulsed laser ablation production of Ni/NiO nano electrocatalysts for oxygen evolution reaction, APL Energy 1 (2023) 016104, https://doi.org/10.1063/5.0144600.
[50] I.G. Casella, M.R. Guascito, M.G. Sannazzaro, Voltammetric and XPS investigations of nickel hydroxide electrochemically dispersed on gold surface electrodes, J. Electroanal. Chem. 462 (1999) 202–210, https://doi.org/10.1016/S0022-0728(98)00413-6.
[51] X. Xu, L. Li, J. Huang, H. Jin, X. Fang, W. Liu, N. Zhang, H. Wang, X. Wang, Engineering Ni^{3+} Cations in NiO Lattice at the Atomic Level by Li^+ Doping: The Roles of Ni^{3+} and Oxygen Species for CO Oxidation, ACS Catal. 8 (2018) 8033–8045, https://doi.org/10.1021/acscatal.8b01692.
[52] O.V. Nestroinaia, I.G. Ryltsova, O.E. Lebedeva, Effect of synthesis method on properties of layered double hydroxides containing Ni (III), Crystals 11 (2021) 1429, https://doi.org/10.3390/cryst11111429.
[53] K.V. Manukyan, A.G. Avetisyan, C.E. Shuck, H.A. Chatilyan, S. Rouvimov, S. L. Kharatyan, A.S. Mukasyan, Nickel oxide reduction by hydrogen: kinetics and structural transformations, J. Phys. Chem. C. 119 (2015) 16131–16138, https://doi.org/10.1021/acs.jpcc.5b04313.
[54] M. Qi, L. Fan, Y. Shen, H. Zou, X. Tian, D. Liu, S. Li, Improved visible-light-induced photocatalytic performance of ZnAl layered double hydroxide by incorporation of Ni^{2+}, J. Nanosci. Nanotechnol. 18 (2017) 753–760, https://doi.org/10.1166/jnn.2018.13940.
[55] F. Wang, S. Chang, Y. Zhao, H. Yang, Y. Zhang, Fabricating highly-active Ni3+ sites of spinel to enhance electrocatalysis oxygen evolution reaction, Int. J. Hydrog. Energy 71 (2024) 8–13, https://doi.org/10.1016/j.ijhydene.2024.05.187.
[56] A. Gulino, I. Fragalà, Cobalt hexafluoroacetylacetonate polyether adducts for thin films of cobalt oxides, Inorg. Chim. Acta 358 (2005) 4466–4472, https://doi.org/10.1016/j.ica.2005.07.031.
[57] A. Gulino, G.G. Condorelli, P. Mineo, I. Fragalà, An x-ray photoelectron spectra and atomic force microscopy characterization of silica substrates engineered with a covalently assembled siloxane monolayer, Nanotechnology 16 (2005) 2170–2175, https://doi.org/10.1088/0957-4484/16/10/033.
[58] A. Gulino, F. Lupo, G.G. Condorelli, M.E. Fragalà, M.E. Amato, G. Scarlata, Reversible photoswitching of stimuli-responsive Si(100) surfaces engineered with an assembled 1-cyano-1-phenyl-2-[4′-(10-undecenyloxy)phenyl]- ethylene monolayer, J. Mater. Chem. 18 (2008) 5011–5018, https://doi.org/10.1039/b809037h.
[59] M. Thommes, K. Kaneko, A.V. Neimark, J.P. Olivier, F. Rodriguez-Reinoso, J. Rouquerol, K.S.W. Sing, Physisorption of gases, with special reference to the evaluation of surface area and pore size distribution (IUPAC Technical Report), Pure Appl. Chem. 87 (2015) 1051–1069, https://doi.org/10.1515/pac-2014-1117.
[60] S. Podila, H. Driss, S.F. Zaman, A.M. Ali, A.A. Al-Zahrani, M.A. Daous, L.A. Petrov, MgFe and Mg–Co–Fe mixed oxides derived from hydrotalcites: highly efficient catalysts for CO_x free hydrogen production from NH_3, Int. J. Hydrog. Energy 45 (2020) 873–890, https://doi.org/10.1016/j.ijhydene.2019.10.107.
[61] Z. Qin, X. Wang, L. Dong, T. Su, B. Li, Y. Zhou, Y. Jiang, X. Luo, H. Ji, CO_2 methanation on Co/TiO_2 catalyst: effects of Y on the support, Chem. Eng. Sci. 210 (2019) 115245, https://doi.org/10.1016/j.ces.2019.115245.
[62] M. Nguyen-Quang, F. Azzolina-Jury, B. Samojeden, M. Motak, P. Da Costa, On the influence of the preparation routes of NiMgAl-mixed oxides derived from hydrotalcite on their CO_2 methanation catalytic activities, Int. J. Hydrog. Energy 47 (2022) 37783–37791, https://doi.org/10.1016/j.ijhydene.2022.08.278.
[63] D. Schmider, L. Maier, O. Deutschmann, Reaction kinetics of CO and CO_2 methanation over nickel, Ind. Eng. Chem. Res. 60 (2021) 5792–5805, https://doi.org/10.1021/acs.iecr.1c00389.
[64] U. JRen, H. Guo, J. Yang, Z. Qin, J. Lin, Z. Li, Insights into the mechanisms of CO_2 methanation on Ni(111) surfaces by density functional theory, Appl. Surf. Sci. 351 (2015) 504–516, https://doi.org/10.1016/j.apsusc.2015.05.173.
[65] G. Dativo, M. Condorelli, G. Compagnini, G. Impellizzeri, S. Scirè, R. Fiorenza, CO_2 conversion by solar photothermo co-catalysis on montmorillonite-based catalysts, Discov. Appl. Sci. 7 (2025) 186, https://doi.org/10.1007/s42452-025-06622-0.